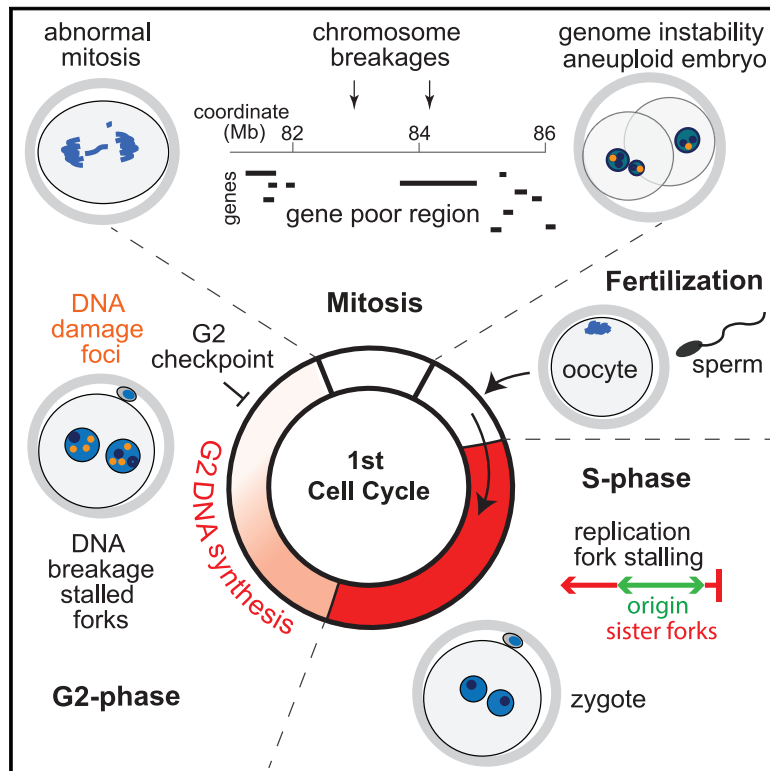


Replication stress impairs chromosome segregation and preimplantation development in human embryos

Graphical abstract



Authors

Katherine L. Palmerola, Selma Amrane, Alejandro De Los Angeles, ..., Amnon Koren, Timour Baslan, Dieter Egli

Correspondence

de2220@cumc.columbia.edu

In brief

In human preimplantation embryos, DNA replication in G2 phase results in chromosome breakage, segmental aneuploidies, and poor embryo quality.

Highlights

- 1-cell embryos show replication fork stalling, with replication extending into G2 phase
- Incompletely replicated DNA is converted to chromosome breaks and aneuploidy in mitosis
- Spontaneous chromosome breaks and G2 DNA synthesis occur in congruent gene-poor regions
- Chromosome fragility in human embryos occurs independently of embryonic genome activation

Article

Replication stress impairs chromosome segregation and preimplantation development in human embryos

Katherine L. Palmerola,^{1,7} Selma Amrane,^{1,7} Alejandro De Los Angeles,^{2,7} Shuangyi Xu,^{2,3,7} Ning Wang,^{2,7} Joao de Pinho,¹ Michael V. Zuccaro,² Angelo Tagliatela,⁴ Dashiell J. Massey,⁵ Jenna Turocy,¹ Alex Robles,¹ Anisa Subbiah,¹ Bob Prosser,¹ Rogerio Lobo,¹ Alberto Ciccina,⁴ Amnon Koren,⁵ Timour Baslan,^{6,7} and Dieter Egli^{1,2,8,*}

¹Department of Obstetrics and Gynecology, Columbia University, New York, NY 10032, USA

²Department of Pediatrics and Naomi Berrie Diabetes Center, Columbia Stem Cell Initiative, Columbia University, New York, NY 10032, USA

³Masters of Biotechnology Program, Columbia University, New York, NY 10027, USA

⁴Department of Genetics and Development, Herbert Irving Comprehensive Cancer Center, Columbia University, New York, NY 10032, USA

⁵Department of Molecular Biology and Genetics, Cornell University, Ithaca, NY 14853, USA

⁶Cancer Biology and Genetics Program, Memorial Sloan Kettering Cancer Center, New York, NY 10065, USA

⁷These authors contributed equally

⁸Lead contact

*Correspondence: de2220@cumc.columbia.edu

<https://doi.org/10.1016/j.cell.2022.06.028>

SUMMARY

Human cleavage-stage embryos frequently acquire chromosomal aneuploidies during mitosis due to unknown mechanisms. Here, we show that S phase at the 1-cell stage shows replication fork stalling, low fork speed, and DNA synthesis extending into G2 phase. DNA damage foci consistent with collapsed replication forks, DSBs, and incomplete replication form in G2 in an ATR- and MRE11-dependent manner, followed by spontaneous chromosome breakage and segmental aneuploidies. Entry into mitosis with incomplete replication results in chromosome breakage, whole and segmental chromosome errors, micronucleation, chromosome fragmentation, and poor embryo quality. Sites of spontaneous chromosome breakage are concordant with sites of DNA synthesis in G2 phase, locating to gene-poor regions with long neural genes, which are transcriptionally silent at this stage of development. Thus, DNA replication stress in mammalian preimplantation embryos predisposes gene-poor regions to fragility, and in particular in the human embryo, to the formation of aneuploidies, impairing developmental potential.

INTRODUCTION

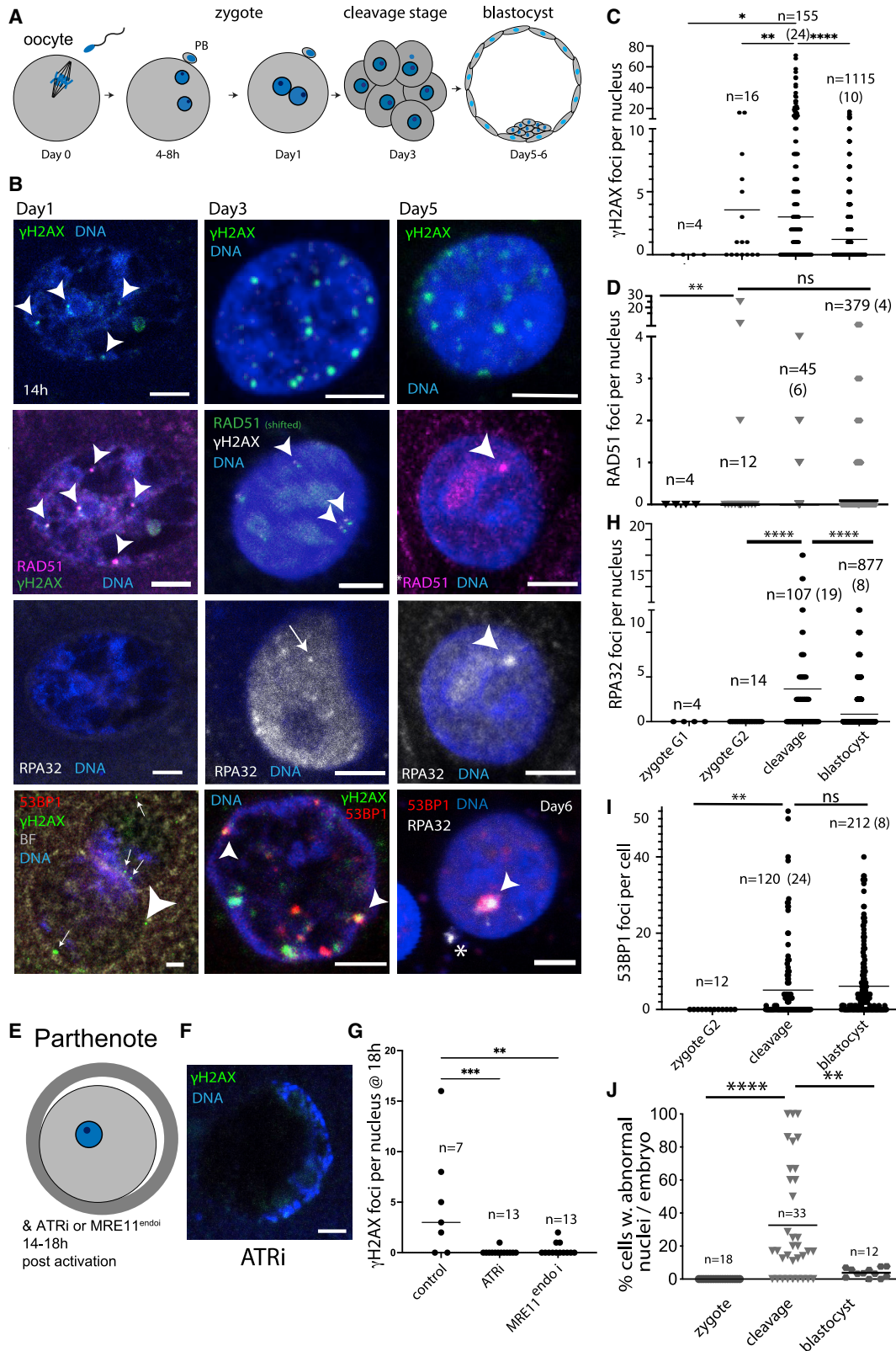
Human reproduction is remarkably inefficient, with abnormalities in the karyotype thought to be an important cause of developmental failure. Human embryos commonly acquire chromosomal abnormalities during mitosis (Vanneste et al., 2009), but the mechanism of their formation is poorly understood. We have recently shown that a double-strand break (DSB) introduced by Cas9 results in both whole as well as segmental chromosomal aneuploidies (Zuccaro et al., 2020). DSBs observed as segmental chromosome aneuploidies may also arise spontaneously and contribute to aneuploidy (Daphnis et al., 2008; Babariya et al., 2017). Arresting aneuploid human embryos generated through *in vitro* fertilization (IVF) upregulate the expression of growth-arrest- and DNA-damage-inducible 45 (GADD45) family genes (Vera-Rodriguez et al., 2015), which are induced in response to various forms of DNA damage and mediate cell-cycle arrest in G2 phase (Wang et al., 1999). Therefore, spontaneous DNA damage in human embryos affects cell-cycle progression and contributes to embryo attrition. A large body of literature demonstrates a strong correlation between mitotic cell-cycle progression, ploidy, the quality of the blastocysts formed, and successful implantation

(Aguilar et al., 2014; Coticchio et al., 2018; Chavez et al., 2012; Van Montfoort et al., 2004; Lee et al., 2012; Fenwick et al., 2002; Sakkas et al., 1998; Shapiro et al., 2000). IVF clinics worldwide grade the quality of cleavage- and blastocyst-stage embryos based on morphological criteria reflecting cell-cycle progression. These criteria have prognostic value and guide decisions on whether or not to transfer embryos (Richardson et al., 2015; Racowsky et al., 2010). Interestingly, embryos with segmental aneuploidy are of lower quality than those without (Escribà et al., 2019). However, how spontaneous chromosomal breaks form and are repaired in the human embryo has not been investigated through controlled experimentation. Furthermore, the location of spontaneous breaks in the genome has not been mapped to genomic coordinates, which could provide insight into the mechanisms of their formation.

RESULTS

Spontaneous DNA damage forms during the first cell cycle in human embryos

The first cell cycle in human progresses within a 1-day window from fertilization to mitosis. To distinguish DNA damage inherited



(legend on next page)

from the gamete versus DNA damage acquired during cell-cycle progression, we stained zygotes on day 0, shortly after fertilization and pronucleus formation, as well as on day 1, shortly before the first mitosis (Figure 1A). No foci for γ H2AX or RAD51 were seen at 1–2 h post pronuclear appearance, but both γ H2AX foci and RAD51 foci were found on day 1 and shortly before mitosis in human zygotes (Figures 1B–1D). The phosphorylation of γ H2AX at Ser139 can be mediated through the activation of ATR kinase, which is activated in response to DNA replication stress (Ward and Chen, 2001). When parthenogenetically activated oocytes were incubated in ATR (ataxia telangiectasia and Rad3-related protein) inhibitor from 14–18 h into the first cell cycle, the number of γ H2AX foci was reduced significantly relative to controls evaluated at the same time point (Figures 1E–1G). Therefore, foci indicating DNA damage and repair form *de novo* after the first S phase. These foci may be DSBs at collapsed replication forks or ssDNA gaps that emerge at stalled replication forks or at lesions behind the fork (Petermann et al., 2010; Kuo and Yang, 2008; Piberger et al., 2020). MRE11 binds to DSBs at stalled forks and at ssDNA gaps to mediate resection, the formation of ssDNA tracts, and the loading of RPA and Rad51 to initiate repair (Piberger et al., 2020; Shibata et al., 2014). We inhibited MRE11 endonuclease activity using PFM01 (Shibata et al., 2014). In the presence of PFM01, the formation of γ H2AX and Rad51 foci was inhibited (Figures 1G and S1A). Thus, γ H2AX and Rad51 foci in G2 phase zygotes represent DNA breaks or gaps that undergo MRE11-dependent processing and activate ATR signaling.

We also stained cleavage stage and blastocyst stages human embryos (Figures 1A and 1B). Foci for γ H2AX increased significantly at the cleavage stage (Figure 1C), whereas RAD51 foci remained constant (Figure 1D). Foci for RPA32, indicating extensive ssDNA (Raderschall et al., 1999), were first observed at the cleavage stage and decreased at the blastocyst stage (Figure 1H). Consistent with ATR activation, RPA32 was found phosphorylated at serine S33 (Figures S1B–S1D), as well as at S4 and S8 (Figures S1E and S1F). RPA32 S33 phosphorylation is conferred by ATR (Vassin et al., 2009), whereas S4 and S8 are phosphorylated at DSBs by DNA-PK or ATM in dependence on S33 phosphorylation (Anantha et al., 2007; Liu et al., 2012; Liaw et al., 2011). Phosphorylation of RPA32 S33 was found in embryos fertilized by either intracytoplasmic sperm injection (ICSI) or by *in vitro* fertilization (Figure S1D) and was particularly notable in binucleated cells and in micronuclei (Figure S1B).

Furthermore, the phosphorylation of CHK1 at serine 317, a checkpoint kinase phosphorylated by and acting downstream of ATR (Liu et al., 2000), was also observed (Figures S1G–S1I).

53BP1 foci smaller than 1 μ m that mark DSBs (Schultz et al., 2000) were absent on days 1 and 2 of development and increased significantly on day 3 (Figures 1I and S1J–S1L). Interestingly, 53BP1 bodies larger than 1 μ m in diameter (Figure S1L) were most common in blastocyst-stage embryos (Figure S1N), present in ~20% of cells (Figure S1O). The 53BP1 bodies indicate sites of repair of incompletely replicated DNA from the previous S phase passed on to daughter cells (Lukas et al., 2011; Harrigan et al., 2011), which is apparent in the symmetry of 53BP1 bodies (Figure S1M), and the presence of RPA32 marking ssDNA (Figures 1B, bottom right, and S1M). The developmental timing of 53BP1 foci formation may be due to the absence of detectable RNF168 transcripts prior to embryonic genome activation (EGA) (Figure S1P); RNF168 is required for the formation of 53BP1 foci at DSBs (Bohgaki et al., 2011; Doil et al., 2009).

Abnormal nucleation, defined by the presence of multiple nuclei within a single blastomere, paralleled the formation of RPA32 foci; although no abnormal nucleation was observed at the zygote stage, it was most common on day 3 at the cleavage stage and decreased at the blastocyst stage (Figure 1J). Chromatin bridges, indicative of unresolved replication intermediates at mitosis, were also observed in cleavage-stage and blastocyst-stage embryos (Figures S1Q and S1R).

Thus, DNA damage is acquired *de novo* during the first cell cycle and at subsequent cleavage divisions. The formation of ssDNA, micronucleation, chromatin bridges, Rad51 foci, 53BP1 foci, and 53BP1 bodies and the phosphorylation of H2AX, RPA32, and CHK1 in preimplantation development are consistent with DNA replication stress, DSBs or a combination of breaks and ssDNA gaps, and with late or incomplete replication at entry into mitosis.

CHK1 delays mitotic entry in response to unreplacated DNA in G2-phase human zygotes

Spontaneous DNA damage can arise during S phase and thus we aimed to understand S-phase progression in human zygotes. We incubated human zygotes with EdU in hourly intervals after fertilization beginning after pronucleus formation (Figure 2A). Pronucleus (PN) formation occurred between 4 and 7.5 h post ICSI (Figure S2A). EdU staining was noted from 6 to 13 h post ICSI but not after 14 h or more (Figure 2A). Therefore, S phase

Figure 1. Markers of DSBs in human embryos arise in the first G2 phase in an ATR-dependent manner

- (A) Schematic of developmental stages.
 (B) Immunostaining for γ H2AX, RAD51, RPA32, and 53BP1 (top to bottom) at indicated stages. Arrowheads indicate co-localization of different markers in the same cell. * indicates micronucleus.
 (C and D) Quantification of nuclear foci at indicated stages for (C) γ H2AX, (D) RAD51. Horizontal bar: mean. The number of cells and embryos (in parenthesis) is indicated.
 (E) Schematic of the experiment. Parthenogenetic (maternal-only) zygotes are made by artificial activation and incubated in ATR inhibitor or MRE11 endonuclease inhibitor during G2 phase.
 (F and G) Immunocytochemistry (F) and quantification (G) of γ H2AX foci at the 1-cell stage 18 h into the first cell cycle with the indicated inhibitor. Horizontal bar, median.
 (H and I) Quantification of nuclear foci at indicated stages. Horizontal bar: mean. The number of cells and embryos (in parenthesis) is indicated.
 (J) Quantification of abnormal nucleation in zygotes, cleavage, and blastocyst embryos. Horizontal bar, mean. Scale bars, 5 μ m. **** $p < 0.0001$, *** $p < 0.001$, ** $p < 0.001$, * $p < 0.05$. Statistical analysis using one-way ANOVA.
 See also Figure S1.

is 6–7 h in human zygotes (Figure 2B). Mitotic entry occurred between 20 and 27 h post ICSI in 19 of 20 zygotes with an average of 24 h (Figure 2C). Human parthenotes ($n = 22$) were generated by an activation pulse. Pronuclei formed at 4 h post activation (Figure S2B), and all human parthenotes (15/15) were in mitosis by 22 h (Figure 2C). Thus, the longest phase of the cell cycle is G2, lasting 8–14 h (Figure 2B). DNA damage foci observed on day 1 in human zygotes are in G2 phase cells, suggesting a continued requirement for DNA synthesis and/or repair.

In addition to EdU staining, we determined the timing of DNA replication completion by applying aphidicolin and monitoring mitotic progression. Aphidicolin introduces replication fork stalling by reversibly inhibiting B-type family DNA polymerases (Ikegami et al., 1978; Wright et al., 1994). Oocytes were activated by parthenogenesis, which allows the synchronous progression through the first cell cycle. Incubation with aphidicolin at 14 h prevented mitotic entry, whereas incubation at 15.5 h allowed mitotic entry with a delay compared with controls (Figure 2C). Incubation with aphidicolin at 18 h had no effects on mitotic entry timing. In the presence of aphidicolin from 15.5 h post activation, foci for γ H2AX and RPA32 formed within 6 h (Figure 2D). The ssDNA bound by RPA32 at remodeled forks activates an ATR-dependent checkpoint (Zou and Elledge, 2003). In the presence of an inhibitor of ATR kinase or of CHK1 kinase from 15.5 h post activation, zygotes entered mitosis with normal timing despite aphidicolin exposure (Figure 2C). Thus, DNA synthesis by replicative DNA polymerase continues at least until 15–16 h post activation, concordant with the presence of spontaneous DNA damage foci. Incompletely replicated DNA delays entry into mitosis in an ATR- and CHK1-dependent manner.

To determine whether CHK1 kinase controls the timing of mitotic entry, we used both ICSI as well as parthenogenetic activation and incubated 1-cell embryos in one of two different CHK1 inhibitors, starting at 15 h. CHK1 inhibition advanced mitotic entry by 4 h, from 24 to 20.3 h in fertilized zygotes and from 21.7 to 17.25 h in parthenotes to as early as 16 h (Figure 2E). CHK1 inhibition in G2 phase was detrimental to genome stability: 9/9 stained zygotes formed abnormal nuclei marked by γ H2AX foci after mitotic exit and failed cytokinesis (Figure 2F). Although most control 2-cell embryos were euploid (12/16 blastomeres), CHK1 inhibition specifically in G2 phase resulted in a high degree of aneuploidy that was further amplified through the addition of aphidicolin (Figure 2G). And when CHK1 was inhibited in day-3 cleavage-stage embryos of 7–8 cells, no cavitation occurred (0/9 embryos), while 3/5 control embryos did undergo cavitation on day 6 of development ($p < 0.05$, Fisher's exact test). CHK1 inhibition in cleavage-stage embryos also resulted in cells containing multiple micronuclei with γ H2AX foci (Figure S2C).

Asymmetric sister fork progression, low replication fork speed, and G2 replication in the first cell cycle

To better understand the first S phase in mammalian zygotes, we also used mice. Murine DNA replication occurs between 4 and 10 h post fertilization (Bui et al., 2010). Consistent with previous studies on fertilized zygotes, parthenogenetic embryos showed no detectable EdU staining between 10–12 h ($n = 10$) and 12–14 h ($n = 10$) post activation. Mitotic entry of controls

occurred on average at 16 h, defining a G2 phase of ~ 6 h (Figure 2H). As EdU staining of whole zygotes may not detect small segments of labeled DNA, we performed DNA fiber analysis of zygotes incubated in late G2 phase with IdU. IdU incorporation was seen in short segments that were estimated to be several hundred base pairs to ~ 1 kb in length (Figure 2I). These could be termination events, repair of collapsed forks, or gap-filling events.

To evaluate DNA replication fork progression in S phase, we performed sequential labeling using IdU and CldU pulses in S phase. Mouse and human embryos showed very slow replication fork progression at the 1-cell stage, which doubled at the cleavage stage and at the blastocyst stage (Figures 2J–2L). Replication fork speed was increased through PARP inhibition in humans and mice (Figures 2M, 2N, S2D, and S2E). PARP inhibition increases replication fork progression and reduces fork reversal under replication stress (Zellweger et al., 2015; Maya-Mendoza et al., 2018). Frequent asymmetry was found in diverging sister forks, in particular at the zygote stage, indicating fork stalling (Figures 2O, 2P, and S2F). Asymmetry in track length was common in zygotes, less common in 8-cell embryos, and uncommon in blastocyst embryos in mice (Figure S2G). PARP inhibition restored symmetry at the 1-cell stage in both mouse and human (Figures S2H, S2I, and S2J). These data are consistent with DNA replication stress.

As in humans, aphidicolin application in G2 phase of mouse 1-cell embryos inhibited mitotic entry depending on the time point of application (Figure S2L). G2 arrested zygotes formed foci with phosphorylated RPA32 on S33, S4, and S8 and foci for γ H2AX and Rad51 (Figure S3), which formed in an ATR-dependent manner within 2–4 h of fork stalling and resolving within 1–2 h after release from the compound (Figure S3). Both G2 arrest and delay of mitotic entry were dependent on G2 checkpoint kinases CHK1 and ATR (Figures 2Q and S2L). CHK1 inhibition in G2 phase also advanced mitotic entry of mouse 1-cell embryos relative to untreated controls from 16.1 to 15.7 h post activation (Figure 2R).

Notably, aphidicolin-treated human parthenotes reproduced defects recently described in human and bovine embryos associated with an abnormal first mitosis (Cavazza et al., 2021), including a failure to polarize chromosomes in the nucleus (16/17 nuclei in this study) (Figures 2D and S2M). Asynchrony in chromosome condensation and mitotic progression between two nuclei in two 2PN human zygotes was also observed (Figures S2N and S2O).

Spontaneous DSBs result in segmental chromosome loss in human cleavage-stage embryos

Unreplicated sites and DSBs can result in chromosome breakage upon entry into mitosis (reviewed in Mankouri et al. [2013]). Chromosomal analysis provides a means to map sites of spontaneous chromosome breakage, which could provide insight into the location of DNA damage and the causes of aneuploidy.

We first analyzed germinal vesicle (GV) oocytes using single-cell genome sequencing. 11/11 GV oocytes showed normal chromosomal content without losses or gains of whole chromosomes or chromosomal arms (Figures S4A–S4C; Table S1). In

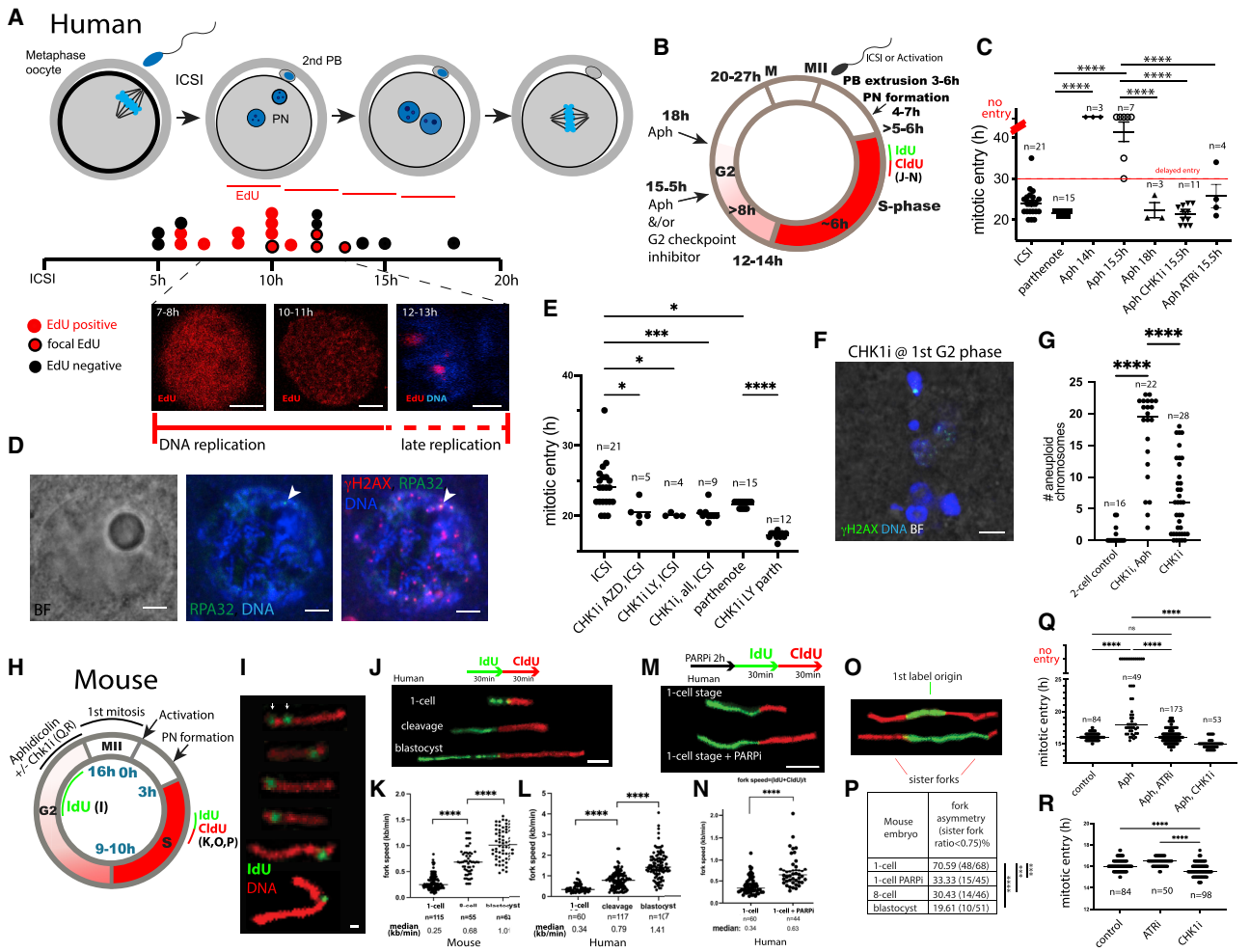
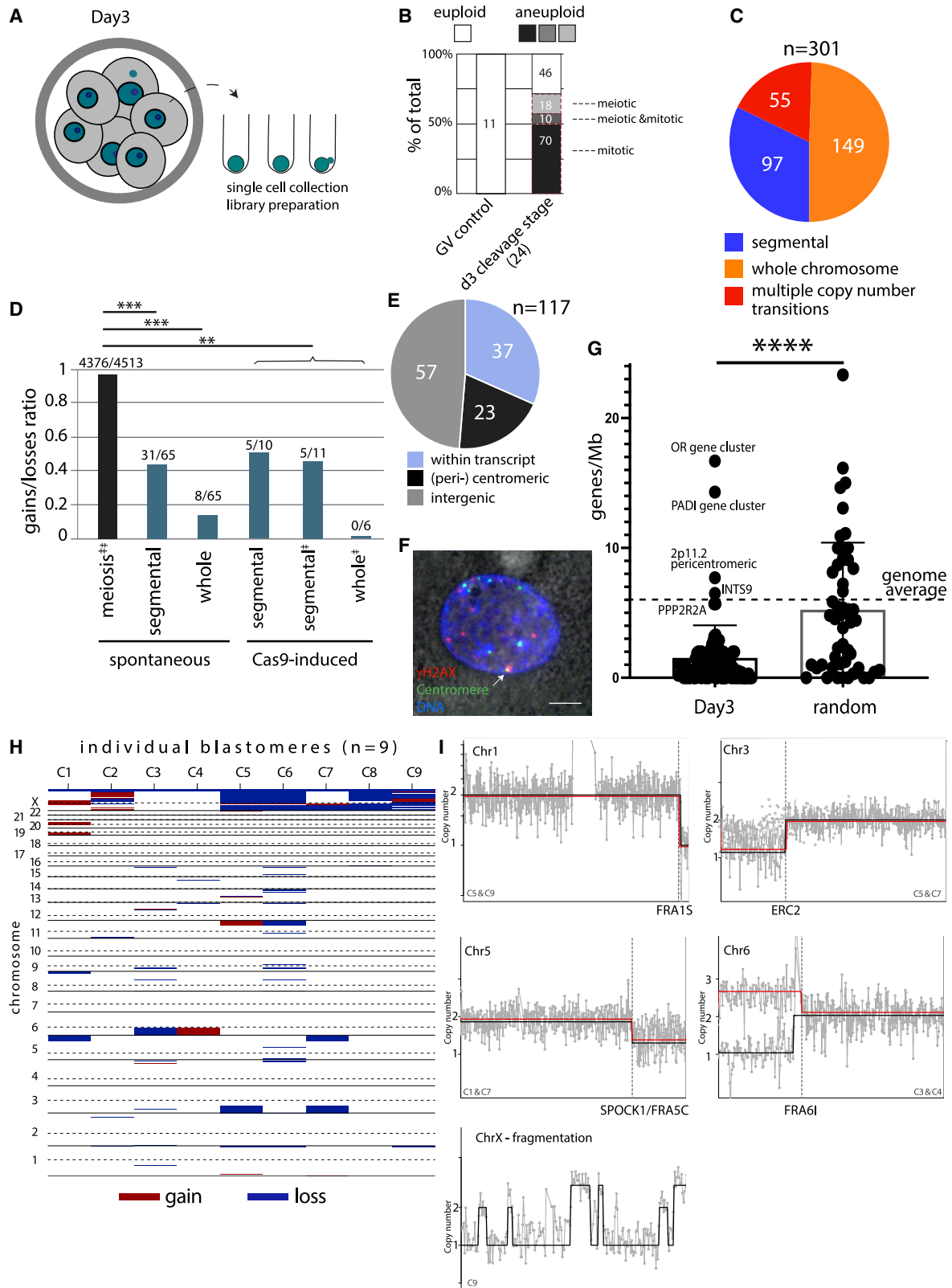


Figure 2. Human and mouse zygotes complete DNA replication in late G2 phase

(A) Following ICSI (time point zero), staggered 1-h pulses of EdU were applied at indicated time points. (B) Schematic of the first cell cycle in human zygotes. The dark red indicates canonical S phase with EdU positive signal. The shaded red indicates DNA synthesis in G2 phase. (C) Timing of mitotic entry (hours post ICSI or activation) in the presence of aphidicolin (Aph) or aphidicolin plus CHK1 inhibitor (CHKi), ATR inhibitor (ATRi), or controls. The number of oocytes is indicated. Statistical analysis using a one-way ANOVA. Horizontal bars, mean; vertical bars, SEM. (D) Immunostaining of human zygotes after 6 h in aphidicolin starting from 15.5 h post activation. (E) Timing of mitotic entry in human zygotes and parthenotes after CHK1 inhibition in G2 phase using either LY2603618 or AZD7762. Horizontal bar, mean. Statistical analysis using one-way ANOVA. (F) Outcome of the first mitosis after CHK1 inhibition in the late G2 phase. (G) The number of aneuploid chromosomes per cell in control 2-cell embryos or after treatment in the late G2 phase with either CHK1 inhibitor alone or in combination with Aph until entry into mitosis. Horizontal bar, median. (H) Timing of the first cell cycle in the mouse. Black, red, and green lines indicate the timing of application of the indicated compound. (I) DNA fiber analysis after IdU incubation in the late G2 phase (at 12–15 h post activation). Scale bars, 1 kb. (J–P) DNA fibers in S phase after sequential pulses of IdU and CldU with quantification. Horizontal bars, median. (J) Representative fibers and the quantification of DNA replication fork track length in mouse (K) and human (L). (M and N) Representative fiber and replication track length after PARP inhibition using Olaparib. (O) An example of sister replication forks from the same origin. (P) The quantification of sister fork asymmetry. **** $p = 0.00001$, *** $p = 0.0001$ using Fisher's exact test. (Q) Timing of mitotic entry in mouse controls and after exposure to indicated inhibitors in the late G2 phase. Horizontal bars, median. (R) Timing of mitotic entry in mouse controls and after Atr or Chk1 inhibition ($n =$ number of embryos). Horizontal bars, median. Scale bars, 5 μ m. See also [Figures S2](#) and [S3](#) and [Table S1](#).

contrast, embryos with Cas9-mediated DSBs showed segmental chromosomal changes at sites targeted by the gRNA ([Figures S4D](#) and [S4E](#); [Table S2](#)), validating methods of analysis.

We analyzed eight 2-cell embryos and identified two segmental aneuploidies in 16 blastomeres ([Table S1](#)). Thus, chromosome breakage is not the secondary consequence a prior abnormal mitosis and can occur spontaneously at the first cell division,



(legend on next page)

consistent with the presence of unreplicated DNA and markers of DNA breakage in G2 zygotes. We then isolated blastomeres from 26 thawed day-3 cleavage-stage embryos (Figure 3A). 145 intact single cells were successfully thawed, collected, and sequenced of which 99 (68%) were aneuploid and 46 (32%) were euploid, and 5/26 embryos (28 cells, 19.5%) showed uniform chromosomal gains or losses, consistent with meiotic origin (Figure 3B; Table S1). 71 cells (49%) were aneuploid due to abnormalities acquired in mitosis characterized by different chromosome content in different cells of the same embryo, and 10 cells contained aneuploidies of both meiotic and mitotic origin (Table S1). We identified a total of 301 chromosomal abnormalities due to mitotic segregation errors, consisting of 97 chromosomes with segmental aneuploidies (32%) with a copy-number change of a chromosome arm (1–2 copy-number transitions), 149 whole-chromosome gains and losses (50%), and 55 events (18%) with 3–10 copy-number transitions on the same chromosome, indicating fragmentation (Figure 3C; Table S1).

Mitotic aneuploidies in day-3 blastomeres showed a net loss of DNA—both segmental losses and whole-chromosome losses outnumbered gains (Figure 3D). This contrasts with chromosomal errors in meiosis, where the ratio of gains/losses approximates 1 throughout preimplantation development (Fransasiak et al., 2014) (Figure 3D). Interestingly, for Cas9-induced chromosome segregation errors, the number of losses also exceeded gains in two different studies (Figure 3D).

Spontaneous chromosome break sites map to gene-poor regions and centromeres

To determine the location of spontaneous chromosomal breaks, we identified regions of copy-number transition. A 2-fold drop or a 50% increase in read number across a chromosomal arm identified the location of a segmental break. We identified a total of 117 chromosomal breaks in blastomeres of day-3 embryos (Table S3). Of these, 57 mapped to intergenic areas, 23 mapped to centromeric and pericentromeric regions, and 37 mapped to gene bodies (Figure 3E). Concordant with the coordinates of chromosomal breaks in day-3 embryos, γ H2AX foci marking DNA breaks were found at centromeres, while the majority located to chromosomal arms (Figure 3F). Gene density at break points was on average 1.5 genes/Mb, lower than at 50 randomly selected sites (Figure 3G; $p < 0.0001$). Only 5 sites had a gene density at genome average (6 genes/Mb) or higher, of which two were gene clusters (Table S3).

Cleavage-stage embryo #4 is representative of the pattern of breakage: segmental breaks were observed in all (9/9) blastomeres, with reciprocal and mirroring copy-number transitions (Figure 3H). Reciprocal events arise from asymmetric chromosome segregation at mitosis, leading to loss and gain in daughter cells (e.g., FRA6I in Figure 3I). Mirroring changes arise from cell-cycle progression of a cell, with aneuploidy acquired in a prior mitosis (e.g., at SPOCK1 in Figure 3I). The division of human blastomeres with broken chromosomes is also seen after Cas9-induced breaks (Figure S4E). Each of the mirroring or reciprocal breaks located to gene-poor regions and common fragile sites (Figure 3I). Segmental losses occurred on chromosome 1 at FRA1S containing the RYR2 gene, at chromosome 3p14.3 containing the ERC2 gene, at FRA5C on chromosome 5 within the SPOCK1 gene, at FRA6I on chromosome 6 near the centromere, and at FRA11O on chromosome 11 within the CNTN5 gene. On the X chromosome, a break at the centromere appears to have preceded the fragmentation of the whole chromosome. Interestingly, transcripts encoded by genes located at these break points were all very long, with SPOCK1 spanning 524 kb, RYR2 792 kb, and ERC2 960 kb and CNTN5 spanning 1,289 kb. No whole-chromosome aneuploidies were observed in this embryo, and thus, chromosome breakage was not the secondary consequence of aneuploidy.

Micronuclei constitute mitotic aneuploidies

The sequencing-based analysis of intact cells provides incomplete resolution, as it is an aggregate signal of different nuclei within the same cell. To circumvent this limitation, we determined the chromosomal content of individually isolated micronuclei. We sequenced 12 individual micronuclei from day-3 blastomeres as well as 18 micronuclei from spontaneously arrested day 5 multicell embryos (Figures 4A and 4B). All micronuclei were aneuploid ($n = 30$) (Figure 4C), including both segmental, whole-chromosome errors, and fragmented chromosomes (Figure 4D). Isolated micronuclei typically were nullisomic for most chromosomes and contained as little as a single chromosome segment (Figure 4E). Break-point mapping in micronuclei isolated from day-3 embryos showed that all ($n = 16$) mapped to gene-poor areas (average 1.1 genes/Mb; Table S3), with gene density lower than random (Figure 4F). 12 break points mapped to chromosomal arms, while 4 (25%) mapped to centromeric and pericentromeric regions. In micronuclei isolated from

Figure 3. Spontaneous chromosome breaks in day-3 embryos map to gene-poor areas and result in chromosome loss

- (A) Experimental schematic. Donated day-3 embryos of good quality were dissociated and individual cells analyzed.
(B) Frequency of euploid and aneuploid cells in day-3 cleavage-stage embryos.
(C) Quantification of error types.
(D) Quantification of gains and losses, displayed as a ratio in spontaneous and Cas9-induced aneuploidies. †† data from meiotic segregation errors from Fransasiak et al. (2014), ‡ data from Zuccaro et al. (2020). *** $p < 0.001$, ** $p < 0.01$ using Fisher's exact test.
(E) Localization of chromosomal break sites.
(F) Immunostaining of day-3 cleavage-stage embryo for γ H2AX and centromeres. Arrow points to the overlap in a single 0.3 μ m confocal section.
(G) Quantification of gene density at chromosomal break sites in comparison to 50 randomly selected sites. The mean and standard deviation are indicated. The dotted line indicates the genome average. Mann-Whitney test **** $p < 0.0001$.
(H and I) Analysis of a 9-cell day-3 embryo of good morphology. (H) The heatmap of chromosomal content of cells 1–9 (C1–C9). (I) Superimposed copy-number plots (red and black lines) of two different blastomeres of the same embryo with reciprocal or mirroring segmental aneuploidies. X chromosome signal of one blastomere only.

See also Figure S4 and Tables S1 and S3.

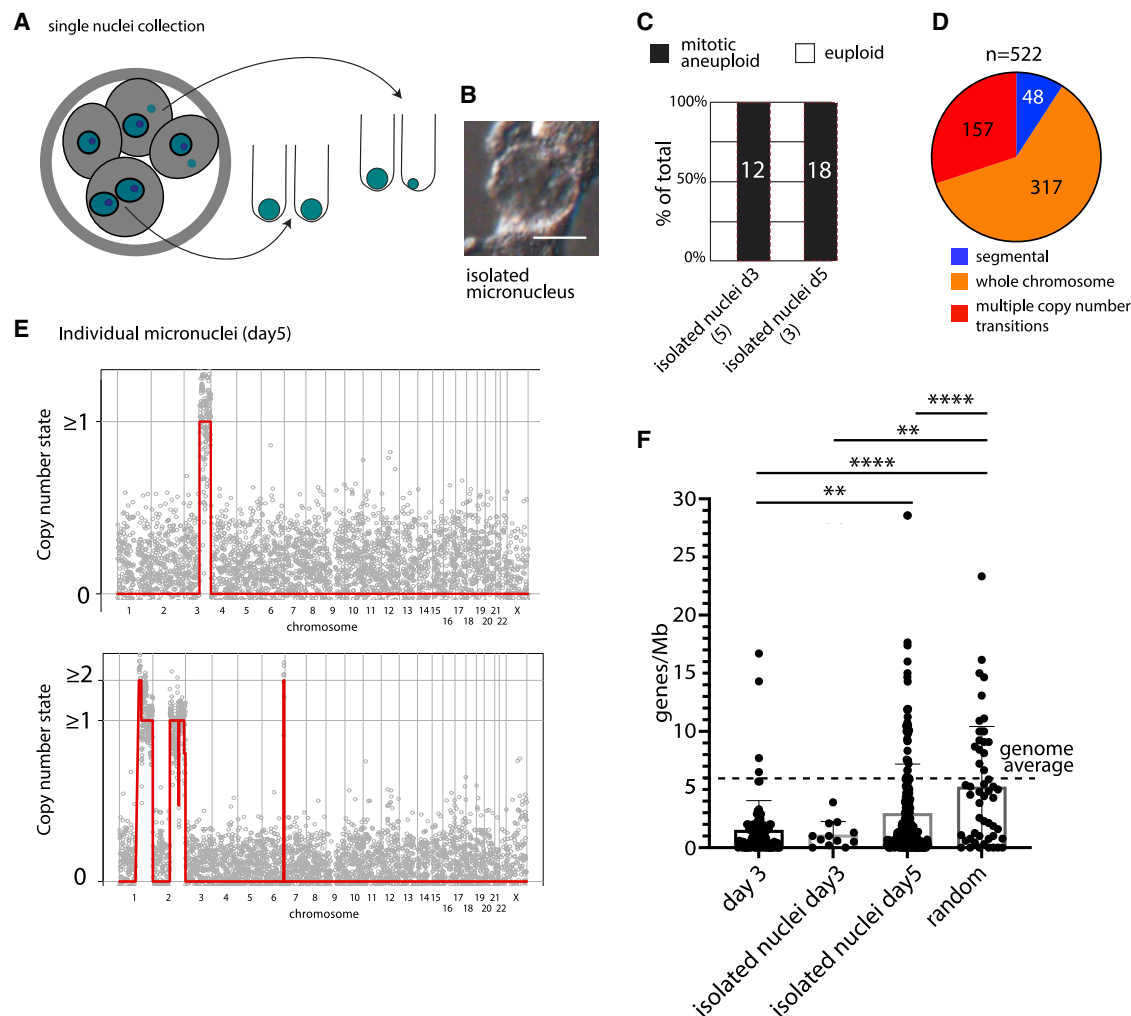


Figure 4. Micronuclei are spontaneous mitotic aneuploidies involving chromosome breakage

(A) Schematic of the experiment. Individual blastomeres are dissociated to individual micronuclei for genome amplification and low-pass sequencing.

(B) Isolated micronucleus. Scale bars, 10 μm .

(C) Ploidy of micronuclei isolated from day-3 or arrested multicell day-5 embryos.

(D) Quantification of the type of abnormalities seen in isolated micronuclei. Nullisomies were counted as whole chromosome aneuploidies.

(E) Representative chromosome content plots.

(F) Analysis of gene density at sites of chromosome breakage. The mean and standard deviation are indicated. The dotted line is the genome average. Mann-Whitney test **** $p < 0.0001$, ** $p < 0.01$.

See also [Tables S1](#) and [S3](#).

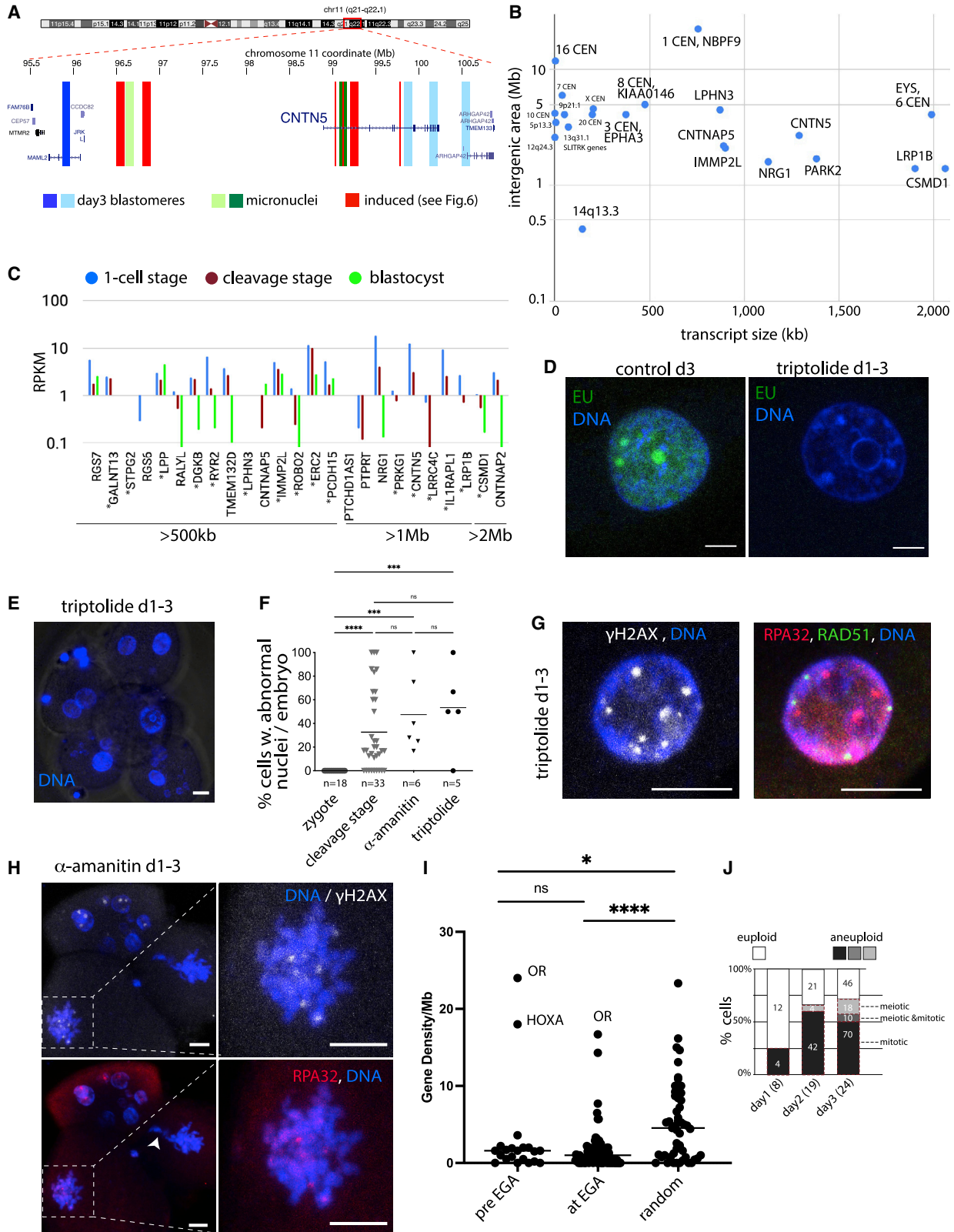
arrested multicell day 5 embryos, 251 break points were mapped ([Table S3](#)). Although gene density at break-point sites was below genome average and random simulated breakage ([Figure 4F](#)), there was an increase in gene-rich sites ([Figure 4F](#)). This increase may be due to the instability of chromosomes in micronuclei ([Crasta et al., 2012](#)), resulting in secondary break points.

Chromosome fragility is independent of embryonic genome activation

Including all break sites identified in day-3 blastomeres, in micronuclei from day-3, and arrested day 5 embryos, we mapped a combined 466 break sites of which 371 were independent events ([Table S3](#)). 154 (42%) were recurrent, locating to 55 different

genomic locations ([Table S3](#)). Recurrence was defined as a breakage in the same genomic region in different embryos. For instance, independent breaks were observed in blastomeres (2 independent breaks) and in micronuclei (2 independent breaks) at the CNTN5 locus and its neighboring intergenic region ([Figure 5A](#)). 22 fragile regions were defined by three or more independent recurrences of which 9 (consisting of 40 independent events) mapped to centromeres and pericentromeric regions, whereas 13 (consisting of 48 independent events [Table S3](#)) mapped to chromosomal arms.

Fragile regions with recurrent breaks harbored either a long transcript or overlapped a large intergenic area ([Figure 5B](#)). 18 of 22 mapped to aphidicolin-sensitive fragile sites identified in



(legend on next page)

somatic cells (Mrasek et al., 2010; Table S3). Chromosome fragility in somatic cells is associated with the expression of long genes in late replicating regions of the genome (Wei et al., 2016), potentially because of conflicts between transcription and replication (Helmrich et al., 2011; Brison et al., 2019; Hamperl et al., 2017).

We determined the expression of long transcripts at the location of recurrent chromosome breaks using published gene expression datasets (Yan et al., 2013). Long fragile site transcripts showed low levels in oocytes and were nearly undetectable at the cleavage stage (Figure 5C; Table S4). Likewise, only 3/37 transcripts of any length that harbored a break site in day-3 cleavage-stage embryos showed upregulation from the 1-cell stage to the cleavage stage (Table S4). Among those 3 transcripts are RAPGEF2 (92-kb transcript), SP3 (57-kb transcript), and NBPF10, which has annotated transcript isoforms of 10 or 1,174 kb. Thus, the expression of neither long nor short transcripts correlates with chromosome fragility in the cleavage-stage embryo.

To directly determine if transcription contributes to embryonic DNA damage and abnormal chromosome segregation in preimplantation embryos, we incubated 2PN zygotes from days 1 to 3 in the presence of α -amanitin ($n = 6$), an inhibitor of RNA polymerase II, or triptolide, an inhibitor of both RNA polymerase I and II ($n = 5$). Cell-cycle progression of human embryos until the 4–8-cell stage does not require transcription, which is inhibited by α -amanitin (Braude et al., 1988; Egli et al., 2011). None of the embryos incubated with triptolide (0/4) showed ethynyl uridine label incorporation, whereas controls did, confirming transcriptional inhibition (Figure 5D). Moreover, no mouse embryos (0/15) developed beyond the two-cell stage in the presence of triptolide, indicating the effective inhibition of EGA, which occurs at the 2-cell stage in mice. Independent of the transcriptional inhibitor, micronucleation, which reflects mitotically acquired aneuploidies, remained comparable with untreated cleavage-stage embryos (Figures 5E and 5F). Furthermore, blastomeres contained foci for both γ H2AX, RAD51, and RPA32 (Figure 5G). The presence of RPA32 foci in mitosis directly demonstrates cell-cycle progression with incompletely replicated single-stranded DNA (Figure 5H).

To determine the location of chromosome breakage prior to EGA, we analyzed the chromosome content of 8 embryos on day 1 of development at the 2-cell stage and 19 embryos on day 2 of development, 17 of which were at the 4-cell stage (Table S3). 2 segmental errors were found in 2-cell embryos within a day of fertilization, and 8 independent segmental errors were found in 67 blastomeres of day-2 embryos. 8 of these were in gene-poor regions, whereas 2 were gene-rich, including the HOXA gene cluster on chromosome 7 and the olfactory receptor gene cluster pericentromeric on chromosome 11. Furthermore, 11 mirroring chromosomal changes in the same day-3 embryo arise through sequential divisions of an error that arose prior to EGA. Gene density at a total of 21 break sites occurring prior to EGA was lower than at simulated random sites (Figure 5I), and the pattern of fragility prior to EGA was the same as at EGA in day-3 embryos. Aneuploidy due to abnormal mitosis was observed in products of all three cleavage divisions on days 1–3 of development, including before EGA (Figure 5J).

Sites of G2 replication are gene poor and concordant with spontaneous chromosome break sites

In somatic cells, gene-poor regions are prone to fragility due to late replication in the cell cycle and entry into mitosis with unrepliated DNA (Le Beau et al., 1998). Notably, 16/25 long fragile site transcripts greater than 500 kb show mitotic DNA synthesis in somatic cell lines (Macheret et al., 2020; Ji et al., 2020) (starred genes in Figure 5C), suggesting that the timing of DNA replication completion may contribute to chromosome fragility of the human embryo.

To map sites of late replication completion in human zygotes, we incubated 6 parthenogenetically activated human embryos with aphidicolin and G2 checkpoint kinase inhibitor at 15.5 h into the first cell cycle (Figure 6A), uniformly resulting in the formation of multinucleate cells (Figure 6B). Individual micronuclei ($n = 25$) were isolated, and 21 from 4 zygotes were successfully sequenced. All contained incomplete genomes (Figure 6C and S5A). The most common aneuploidy was whole-chromosome losses (248 chromosomes, 73%), followed by chromosomes with one or more segmental copy-number transitions (93 chromosomes, 27%) (Figure 6D).

Figure 5. Genome instability is independent of embryonic genome activation

- (A) Fragile chromosome region at FRA110 at the CNTN5 locus with recurrences in blastomeres, micronuclei, and aphidicolin-induced breakage (see Figure 6). Vertical bars indicate break-point positions. The different blue or different green colors indicate independent events observed in different embryos. Adapted from the UCSC genome browser (hg19).
- (B) Size of long transcripts and of intergenic areas overlapping with 22 fragile regions.
- (C) Expression of long transcripts (RPKM) at fragile sites in human preimplantation embryos. No bar is shown when expression is undetectable. * indicates genes with mitotic DNA synthesis in somatic cells (Ji et al., 2020; Macheret et al., 2020). Data from GSE36552 (Yan et al., 2013).
- (D) Staining for ethynyl uridine (EU) labeling nascent transcripts.
- (E) Embryo incubated in triptolide from the 2PN stage to day 3 with abnormal nucleation in 4 of 6 blastomeres.
- (F) Quantification of micronuclei in control IVF embryos and embryos treated with RNA polymerase inhibitor from day1–3. Horizontal line, mean. Statistical analysis using one-way ANOVA. *** $p < 0.001$, **** $p < 0.0001$.
- (G) Immunocytochemistry for indicated markers of DSBs and repair after triptolide treatment.
- (H) Immunostaining for RPA32 and γ H2AX after α -amanitin treatment. Insets show magnification. Note the presence of both RPA32 and γ H2AX foci in the mitotic cell. Scale bars, 10 μ m.
- (I) Gene density at break sites before and at EGA compared with simulated random breakage. Horizontal line, mean. Statistical analysis using Mann-Whitney test. * $p < 0.05$, **** $p < 0.0001$.
- (J) Frequency of aneuploid cells through the first three cell divisions.
- See also Tables S1, S3, and S4.

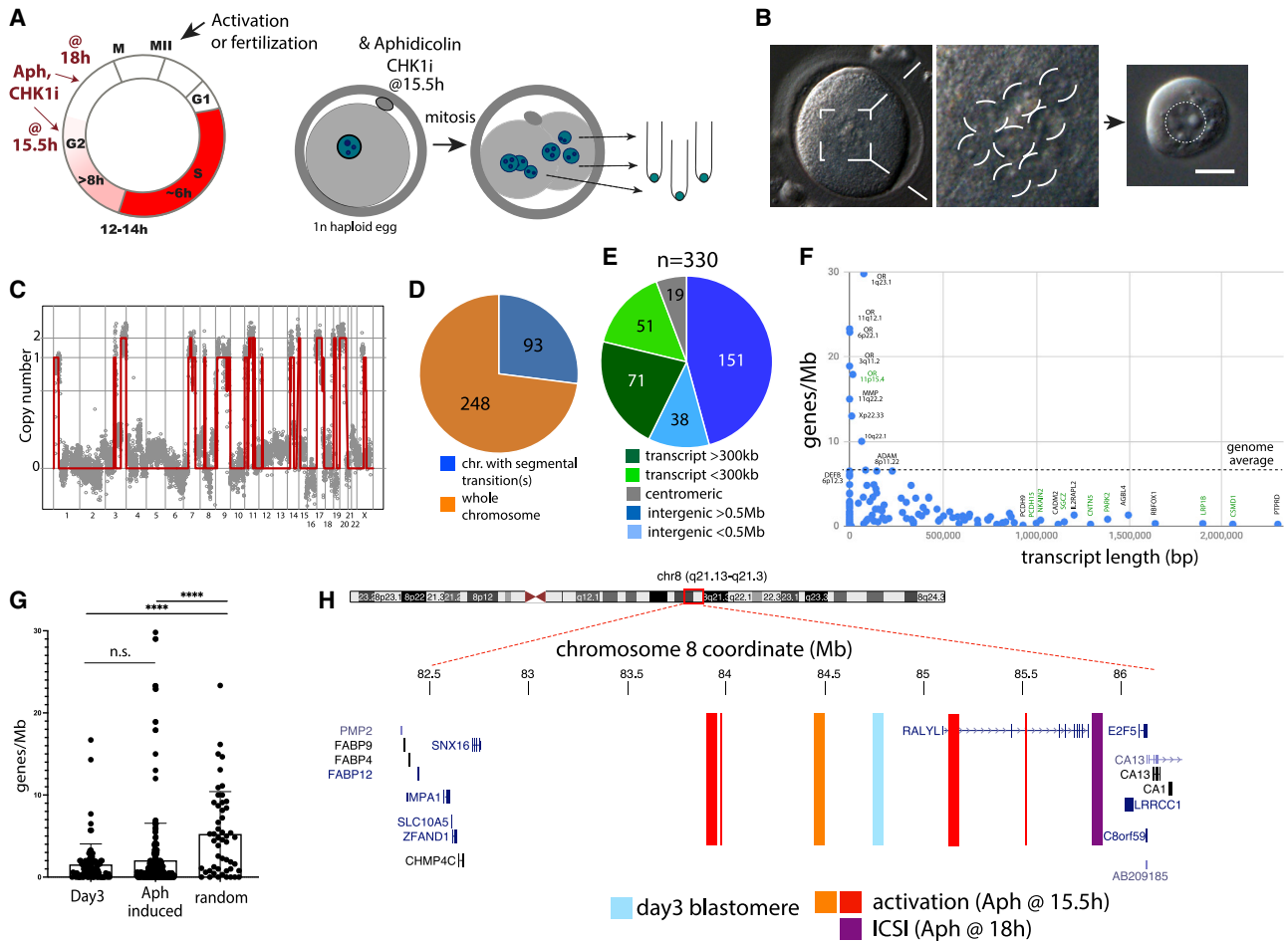


Figure 6. Gene-poor regions require G2 DNA synthesis

(A) Schematic of the experiment. Human zygotes are incubated with DNA polymerase inhibitor aphidicolin and CHK1i in G2 phase. Upon progression through mitosis, micronuclei form, which are harvested individually for sequencing.
 (B) Cell after mitotic entry in the presence of aphidicolin and CHK1i and isolated individual nucleus. Scale bars, 10 μ m.
 (C) Chromosome content plot of an isolated nucleus.
 (D) Quantification of the type of error.
 (E) Genomic characteristics of chromosomal break sites.
 (F) Density of protein-coding genes and size of affected transcription units at break sites. Intergenic sites are at 0 transcript length on the y axis. Break sites at long transcripts or gene-rich regions are indicated. Sites labeled in green are concordant with spontaneous breakage in IVF embryos (Table S3).
 (G) Comparison of gene density at spontaneous, aphidicolin-induced, and random sites. Mean and SEM are indicated. **** $p < 0.0001$ using a Mann-Whitney test.
 (H) Vertical bars indicate the break-point position at the RALYL locus on chromosome 8, in parthenogenetically activated embryos (independent events red and orange with aphidicolin added at 15.5 h post activation), fertilized zygotes (purple with aphidicolin added at 18 h post ICSI), and spontaneous breakage in day-3 blastomeres (blue).

See also Figures S5 and S6 and Tables S1 and S5.

The break-point analysis identified a total of 331 break sites (Table S5). The analysis of polar bodies of the same embryos was performed to exclude a single break of meiotic origin. Of the 330 mitotic break sites, 191 (58%) showed reciprocity in a different nucleus, whereas 139 were singular, consistent with a recovery of chromosomal material per embryo of 59% (Figure S5B; Table S5). Per embryo, an average of 51 independent break points were found, corresponding to at least 51 unrepliated sites. 19 break sites (6%) were centromeric, and 189 break sites were intergenic of which 151 (46%) were located in inter-

genic areas of 0.5 Mb or greater. 122 break sites (37%) located within a transcript of which 71 (21.5%) were longer than 300 kb (Figure 6E). Among the longest genes were PARK2, CNTN5, PTPRD, CSMD1, MDGA2, PCDH9, and PCDH15 (Figure 6F). 184 breaks (56%) were in gene-poor areas of 1 or fewer genes/Mb, and 24 sites (7%) had a gene density at and above the genome average (~ 6.9 genes/Mb). Of these 24 gene-rich sites, 16 (5%) located to gene clusters, in particular to olfactory receptor gene clusters (11) (Figure S5C), metalloproteinase gene clusters MMP (1) and ADAM (1), as well as CYP4 (1) and DEFB (2)

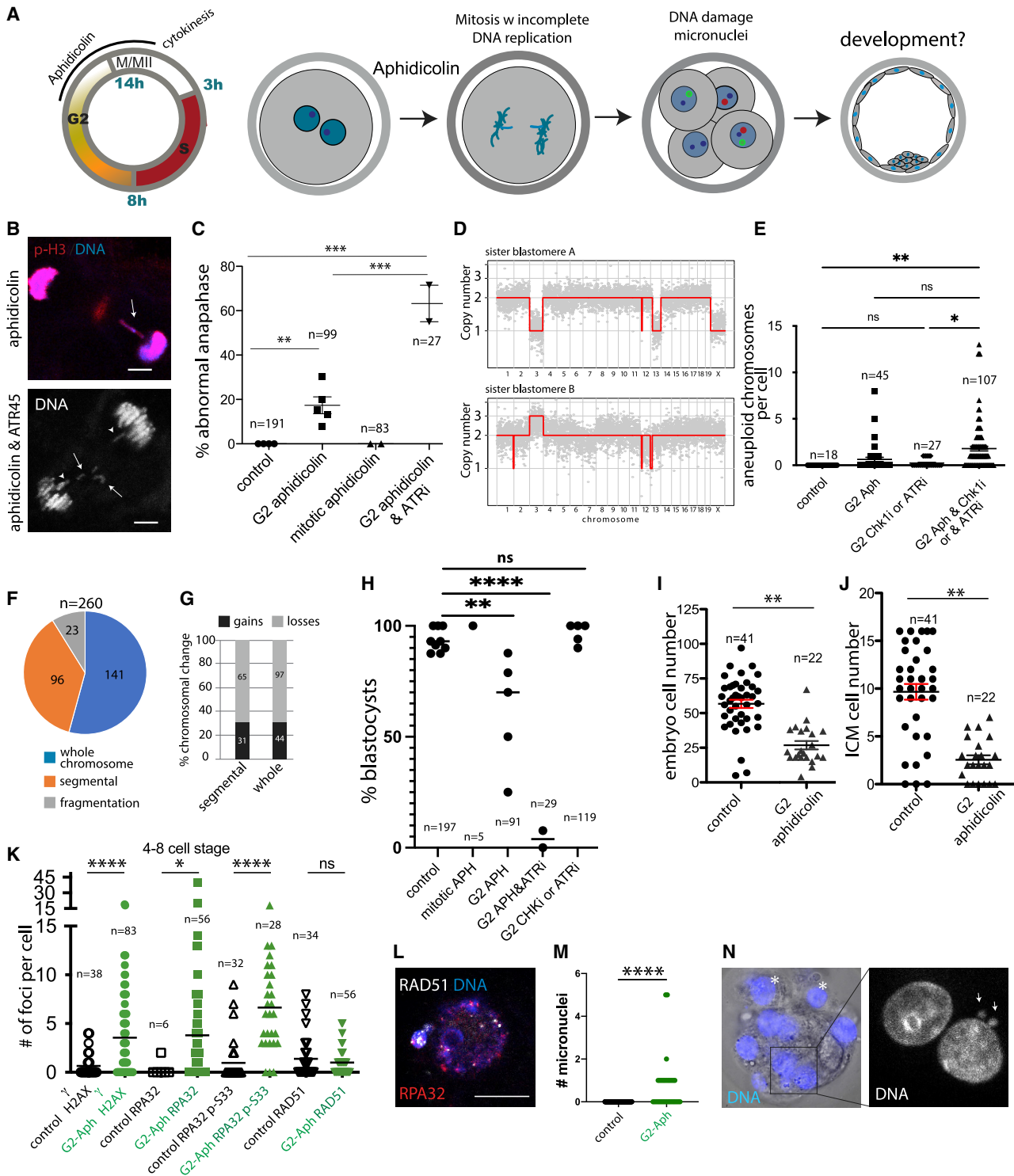


Figure 7. Induced chromosome fragility in late replicating regions compromises developmental potential in mouse embryos

(A) Schematic of timed aphidicolin (Aph) application in G2 of the first cell cycle.

(B) Immunostaining at anaphase of the first mitosis. Arrows indicate chromosomes failing to segregate, arrowheads indicate delayed segregation.

(C) Quantification of abnormal anaphase figures for indicated conditions. Mean with SEM is indicated. Statistical analysis using one-way ANOVA.

(D) Single-cell karyotype analysis of sister blastomeres at the 2-cell stage.

(legend continued on next page)

gene clusters (Figure 6F). The remaining gene-rich areas had adjacent gene-poor regions of more than 0.5 Mb (e.g., SLC30A7 at 1p21.1; Figure S5D). Only one site on chromosome 9q31.3 was not within or immediately adjacent to a gene-poor region. When comparing induced break sites with random simulated breakage, gene density was lower ($p = 1.5e-7$) (Figure 6G). Gene density at aphidicolin-induced break sites and spontaneous breakage in day-3 cleavage-stage embryos were not different (Figure 6G).

Break sites induced by aphidicolin at sites of G2 replication were concordant with spontaneous break sites, such as at CNTN5 on chromosome 11 or RALYL on chromosome 8 (Figures 5A and 6H). Of the 22 fragile regions in untreated embryos, 14 (64%) were also found in the cohort of aphidicolin-induced breaks (Table S3). To evaluate concordance with fertilized embryos, we also incubated 4 2PN zygotes with aphidicolin and CHK1 inhibitor at 18 h post fertilization by ICSI. 7 chromosomal breaks were identified in 4 different genomic locations of which 2 were concordant with break points in parthenogenetically activated oocytes at the centromere on chromosome 9 and at RALYL on chromosome 8 (Figure 6H). Taken together, DNA synthesis continues at least until 18 h of the first cell cycle and into mitotic prophase. Notably, aphidicolin exposure at 18 h did not delay mitotic progression (Figure 2C), despite the presence of at least 2 unreplicated sites per embryo.

To evaluate the potential role of transcription in aphidicolin-sensitive replication delays, we examined the expression of transcripts at break sites (Yan et al., 2013). All but four of 93 transcription units with break sites, EIF3E, UVRAG, GULP1, and CRADD, were either not expressed or transcript levels decreased from the 1-cell stage to the morula stage after EGA (Table S4). Only 3 of 330 break sites (0.9%) located near a transcription start site, and only one of these, CRADD, was expressed at a later developmental stage. Furthermore, we compared embryo break sites with transcription-dependent replication delays described in somatic cells (Sarni et al., 2020). Of the 119 sites identified by Sarni and colleagues, 6 sites were shared at the genes FTO, LAMA2, MAGI2, SCAPER, THSD4, and VPS13B. However, zygotes are transcriptionally largely silent, and none of these genes showed appreciable transcription after EGA (Table S4). We also compared embryo break sites to aphidicolin-induced recurrent break sites in actively transcribed genes of human neuronal progenitors (Wang et al.,

2020). Of 31 sites identified by Wang and colleagues, 10 were shared with the embryo (32%) at CTNNA2, NRG3, RBFOX1, LRP1B, PARK2, MAGI2, LINGO2, DLG2, PCHD15, and LRRD4C. Eight of these ten genes show mitotic DNA synthesis in somatic cells (Ji et al., 2020; Macheret et al., 2020). Again, these genes showed no expression during cleavage development. Thus, the need for DNA synthesis in G2 phase in human zygotes is independent of transcription-replication conflicts.

Fragility in late replicating regions compromises developmental potential

In mice, spontaneous mitotic chromosome segregation errors are less common than in human embryos (Bolton et al., 2016), and preimplantation development is more efficient. Because of the low frequency of spontaneous segregation errors, the mouse lends itself to experimental interference. To determine whether inhibiting G2 replication reproduces the chromosomal and developmental abnormalities seen in human embryos, we applied the DNA polymerase inhibitor aphidicolin in G2 phase (Figure 7A). All 191/191 control parthenogenetic zygotes showed normal chromosome segregation at the first mitosis, whereas 17/99 (17.4%, range per experiment 7%–30%) treated embryos showed abnormal anaphase with lagging chromosomes and chromosome fragments (Figures 7B and 7C). Aphidicolin applied only after pronuclear envelope breakdown was inconsequential (Figure 7C). The frequency of abnormal anaphase figures increased to 63% (16/27) when embryos were exposed to both ATR kinase inhibitor and aphidicolin in G2 phase.

Chromosome content analysis of sister blastomeres at the 2-cell stage showed that 98% of control cells had normal mitotic segregation (57/58), whereas 33% (14/45) of aphidicolin-treated blastomeres showed aneuploidy (Figure 7D; Table S6). The combination of aphidicolin and G2 checkpoint inhibition further increased aneuploidy to 64.5% of the blastomeres (69/107), consistent with the frequency of abnormal anaphases. In aphidicolin-treated samples, a total of 28 chromosomal abnormalities were found in 45 blastomeres, or 0.62 per cell. G2 checkpoint inhibition alone resulted in 0.3 abnormalities per cell (8 aneuploidies in 27 cells). In embryos treated with both aphidicolin and G2 checkpoint inhibitor, aneuploidies increased to 2.1 per cell (226 aneuploidies in 107 cells) (Figure 7E). Karyotype abnormalities included whole-chromosome segregation errors (54%), segmental errors (37%), and chromosome fragmentation (9%)

(E) Quantification of aneuploidies per cell for indicated conditions. G2 checkpoint inhibitor includes ATR inhibition (10 samples) and CHK1 (17 samples; Table S6). Mean with SEM is indicated. Statistical analysis using one-way ANOVA.

(F) Quantification of the types of chromosomal abnormalities at the 2-cell stage. Fragmentation is defined as 3 or more copy-number transitions on the same chromosome.

(G) Percentage of gains and losses.

(H) Percent blastocyst development at indicated conditions. The 119 ATR and CHK1 inhibition samples consist of 57 ATR and 62 CHK1 inhibition. Statistical analysis using one-way ANOVA. Horizontal line, median.

(I and J) Analysis of embryo quality through the quantification of cell number (I) and ICM cell number (Pou5f1 positive cells) (J). Statistical analysis using Student's t test, bars indicate the mean and SEM.

(K–N) Analysis after Aph treatment in G2 phase of the first cell cycle. (K) The quantification of DNA damage markers at the 4–8 cell stage, 48 h post activation. Horizontal bars, mean. Statistical analysis using one-way ANOVA. (L) Immunostaining of the nucleus of a day-4 embryo for indicated DNA damage markers. (M) Quantification of micronuclei per embryo at 48 h post activation. No micronucleation was observed in controls. Statistical analysis using Student's t test. (N) The embryo on day 4 of development with binucleation and micronucleation (magnified), and excluded cells indicated with an asterisk. **** $p < 0.0001$, *** $p < 0.001$, ** $p < 0.01$, * $p < 0.05$.

See also Figures S6 and S7 and Table S6.

(Figure 7F). Whole chromosome as well as segmental losses exceeded gains by a ratio of $\sim 1:2$ (Figure 7G).

Although in controls, 92% of eggs developed to the blastocyst stage, of the cleaved embryos exposed to aphidicolin in G2 phase, 72% developed to the blastocyst stage (range 25%–87%) (Figure 7H), concordant with the frequency of euploid embryos. On day 5 of development, blastocysts obtained after treatment with aphidicolin in G2 showed reduced total cell number and fewer ICM cells marked by Pou5f1, indicating low embryo quality (Figures 7I and 7J). Aphidicolin-treated embryos showed increased markers of DNA damage, including γ H2AX, Rpa32, and Rpa32 phosphoS33 at the 4–8 cell stage at 48 h post activation (Figures 7K and 7L). Embryos were developmentally delayed and showed excluded blastomeres, binucleation, and increased micronucleation (Figures 7M and 7N). Thus, incomplete replication at the first mitosis destabilizes the genome in subsequent cell divisions and phenocopies common spontaneous defects in human embryos.

Response to unreplicated DNA differs between mouse and human embryos

In comparison to human cleavage-stage embryos, untreated mouse embryos showed not only a lower frequency of spontaneous chromosome segregation errors (Figure 7E versus Figure 5J) but also a lower frequency of segregation errors caused by interference with replication completion in G2 phase (Figure 7D versus Figure 6C). Surprisingly, 38 of 107 (35.5%) of mouse 2-cell embryos were euploid despite combined aphidicolin exposure and G2 checkpoint inhibition (Table S6), whereas all human embryos were aneuploid. Mouse embryos showed aneuploidies on just 2 chromosomes per cell, whereas human embryos showed catastrophic aneuploidy with on average 51 break sites or more than one genomic alteration per chromosome. This difference could be due to a lower number of unreplicated sites in mice at the time of inhibitor application or due to differences in the response and resolution of unreplicated DNA.

To estimate the number of unreplicated sites, we counted the number of DNA damage foci induced in G2 phase (Figures S6A–S6G). Aphidicolin incubation resulted in a higher number of γ H2AX and RPA32 foci in mice (mean γ H2AX foci 43, range 0–228, in mice versus human, mean 21, range 0–51). Approximately 10% of γ H2AX foci were positive for RPA32 in both species, which averaged 1.8 in human versus 4.5 in mice per haploid nucleus (Figures S6B and S6D). The processing of DSBs and the extension of ssDNA gaps required for the formation of RPA binding and ATR kinase activation involves the nuclease activities of MRE11. The inhibition of MRE11 exonuclease using mirin results in a repair defect at DSBs and thereby increases the number of DNA damage foci (Dupré et al., 2008; Shibata et al., 2014). The addition of mirin combined with aphidicolin (schematic in Figure S6A) increased the number of foci marked by γ H2Ax in mouse zygotes to more than 100 and the number of Rad51 foci to more than 50 (Figure S6E). The inhibition of MRE11 endonuclease activity abrogated foci for both markers (Figure S6E), suggesting that sites stalled by aphidicolin were processed in an MRE11-dependent manner. An increase in the number of RAD51 foci upon combined exposure to aphidicolin and mirin was also seen in human zygotes, increasing to 50 sites on

average (Figure S6F). The number of γ H2Ax foci was not increased by MRE11 inhibition beyond aphidicolin incubation alone, though it could be an underestimate as large H2Ax bodies may contain multiple sites (Figure S6G). Thus, the number of foci marking unreplicated sites in G2 phase is higher in mice than in human at the relevant time points. The number of aneuploidies induced by aphidicolin incubation exceeds the number of γ H2Ax foci in human, whereas in mice it is the reverse. Thus, human zygotes are less efficient at forming DNA damage foci and more efficient at converting sites of incomplete replication to chromosomal breaks and aneuploidy.

Consistent with differences in the processing of stalled replication forks, transcripts of SMARCAL1, FBH1, RAD51, and Bloom (BLM) were lower in human than in mice, whereas FANCD1/BACH1 was expressed at higher levels (Figure S6H; Table S7). These factors are involved at different steps of replication fork reversion and resection (reviewed in Joseph et al. [2020]) (Figure S6I). In contrast, transcripts for MUS81, which cleaves replication intermediates at prophase of mitosis to form DSBs, were higher in human (Figure S6H). Interestingly, human zygotes progressed to mitotic prophase (16 of 17) with condensed chromatids despite persistent γ H2AX and RPA32 foci (Figures 2D and S2M), whereas mouse zygotes arrested in G2 phase without chromosome condensation (Figure S3). Human cleavage embryos were reported to express low levels of WEE1 kinase (Kiessling et al., 2010), which acts upstream of CDK1 and MUS81 to inhibit cleavage of replication forks that remain stalled late in the cell cycle (Duda et al., 2016). We confirmed low WEE1 transcript levels at the 1-cell stage in human relative to mice (Figure S7A). When Wee1 kinase inhibitor was added alongside aphidicolin to mouse embryos, mitosis resulted in a highly fragmented genome (Figures S7B and S7C; Table S6), reproducing the frequent segmental breakages seen in human embryos. Wee1 kinase inhibition in G2 phase mouse embryos advanced mitosis by 1.5 h and impaired developmental potential compared with untreated controls (Figures S7D–S7F). In summary, inefficient DNA damage foci formation, progression to mitotic prophase with unreplicated DNA, and frequent formation of chromosomal breaks at sites of incomplete replication, followed by an unstable genome during cleavage divisions (Figure S7G) are defining differences between human and mouse preimplantation development.

DISCUSSION

Replication stress in mammalian embryos

Aneuploidy is a major cause of developmental failure in humans, but the origins of mitotic aneuploidies are not well understood. We show here that human embryos acquire DNA damage during embryonic DNA replication, which is characterized by replication fork stalling, DNA synthesis in G2 phase, followed by incomplete replication at mitosis, chromosome breakage, micronucleation, and aneuploidy. A possible cause of replication fork stalling is DNA demethylation, which occurs primarily during the first two cleavage divisions prior to zygotic genome activation (Guo et al., 2014). Foci for γ H2AX indeed form concordant with active DNA demethylation in mouse preimplantation embryos

(Wossidlo et al., 2010). Demethylation may affect DNA replication through the formation of abasic sites and ssDNA breaks that stall replication forks (reviewed in Thompson and Cortez [2020]). The replication of damaged DNA results in reduced replication fork speed (Tercero and Diffley, 2001), including stalling and fork reversal (Iyer and Rhind, 2017; Zellweger et al., 2015). The transcriptional silence of the early embryo during genome demethylation might be a necessary adaptation to avoid additional stress imposed by transcription-replication conflicts. Other potential sources of DNA replication stress are paternal DNA damage (Simon et al., 2011) and a short G1 phase (Ahuja et al., 2016). Paternal and maternal segmental aneuploidies are found in approximately equal frequency (Zuccaro et al., 2020), and slow replication fork speed and G2 replication are also seen in maternal-only embryos, arguing against paternal DNA damage as the primary source of DNA replication stress.

The mapping of spontaneous chromosomal break sites in the human embryo showed that these are typically gene poor, contain a long neural gene, or contain clusters of genes that are transcriptionally silent, such as olfactory receptor genes. These regions require DNA synthesis in G2 phase in the embryo. Gene-poor, fragile regions tend to complete replication late in the cell cycle also in somatic cells (Macheret et al., 2020; Ji et al., 2020; Widrow et al., 1998) and can remain incompletely replicated through mitosis (Moreno et al., 2016). Gene-poor regions may be prone to fragility because of a limiting number of replication origins, as described for somatic cells (Letessier et al., 2011). Future studies on the origin location in embryos will provide answers to this question.

Incomplete replication is known to affect chromosome segregation, chromosome condensation, and spindle function in somatic cells (Burrell et al., 2013; Feng and Jasin, 2017; Wilhelm et al., 2014; Chang et al., 2007). Interestingly, a recent study on human and bovine zygotes describes incomplete chromosome condensation, incomplete polarization of chromatin in the nucleus, and lagging chromosomes at the first cell division (Cavazza et al., 2021). These defects can be conferred by incomplete replication as induced by aphidicolin. Though mitotic abnormalities can also be induced by interference with spindle function by nocodazole (Bolton et al., 2016; Cavazza et al., 2021), this primarily results in whole-chromosome aneuploidies (Bolton et al., 2016) and as a secondary consequence of micronucleation in chromothripsis (Crasta et al., 2012), rather than in the specific patterns of chromosome breakage described here. Replication stress as induced by aphidicolin can also lead to prolonged mitosis, multipolar spindles, and destabilize the segregation of the entire genome (Wilhelm et al., 2014). Multipolar mitosis occurs spontaneously and commonly in human embryos, contributing to developmental failure (Ottolini et al., 2017). Furthermore, prolonged mitosis correlates with aneuploidy and poor developmental potential (Wong et al., 2010). Thus, replication stress can underlie the mitotic abnormalities described by Cavazza, Ottolini, Wong, and colleagues.

Mechanisms and consequences of mitotic aneuploidy differ from meiotic aneuploidy

Mitotic errors predominantly result in the loss of genetic material—gains are underrepresented relative to losses. This asym-

metry persists throughout development: Turner syndrome arises through mosaic loss of one X chromosome (Hook and Warburton, 1983). In contrast, for meiotic errors, the ratio of losses/gains approximates 1 throughout preimplantation development (Franasiak et al., 2014) and gains exceed losses in live births. Further differences in meiotic versus mitotic errors are seen in which chromosomes are affected. Segmental chromosome breaks primarily affect large chromosomes (Girardi et al., 2020; Escribà et al., 2019; Zhou et al., 2018), whereas meiotic aneuploidies primarily affect smaller chromosomes, at least at advanced maternal age (Gruhn et al., 2019). Furthermore, mitotic segregation errors inflict damage to the affected chromosome through breakage and fragmentation and thereby, commonly result in a chromosomal loss, as well as the demise of the affected cell or embryo. In contrast, segregation errors in meiosis can result in stable chromosomal gains and continued development.

Replication stress impacts human reproduction

Chromosome segregation errors and aneuploidy are one of several possible outcomes of stalled replication forks and DSBs. In somatic cells, fragile sites are hotspots of *de novo* copy-number variation (Wilson et al., 2015). Chromosomal break sites observed here coincide with sites of *de novo* copy-number change that can cause disease, including at GALNT13, IMMP2L, RGS7, and CHRM3 (Shimajima et al., 2017; Cheng et al., 2019; van Bever et al., 2005; Gimelli et al., 2014; Perrone et al., 2012). Whether these genetic changes occurred prior to or after fertilization is not known. Genetic mosaicism in the placenta, as well as mosaicism in adult tissues, points to early embryonic cell cycles as a source of frequent genetic change (Coorens et al., 2021; Ju et al., 2017; Rodin et al., 2021). In the placenta, the majority of copy-number changes occur at fragile sites, including at sites of direct concordance with breakpoints in human preimplantation embryos, such as within IMMP2L, and may thus originate through the processes described here. Stalled replication forks and replication gaps may also contribute to point mutations through completion of DNA synthesis with error-prone translesion polymerases.

Taken together, DNA damage incurred during DNA replication underlies common defects in early human development, providing a rationale for additional studies on the limiting factors involved in replication fork stability and DSBs repair, on the location of replication origins, and the temporal patterns of DNA replication, as well as on the molecular causes of DNA replication stress in the early embryo. Such studies will be critical for understanding both normal and disease-causing genetic variation in the human germ line. Long term, it may lead to methods to reduce the risk of genetic abnormalities and reduce embryo attrition in human reproduction.

Limitations of study

Stalled replication forks and postreplicative ssDNA gaps can both activate ATR signaling and involve MRE11-dependent processing. This study does not distinguish between these different possibilities. Such distinction may be achieved through the electron microscopy of replicated DNA or through S1 nuclease assays.

While this study was under consideration, another study reported low replication fork speed in fertilized mouse 2-cell and 8-cell embryos (Nakatani et al., 2022). Moreover, another study showed in somatic cells that G2 DNA synthesis is a replication stress response to low fork speed induced by aphidicolin (Mocanu et al., 2022).

STAR★METHODS

Detailed methods are provided in the online version of this paper and include the following:

- **KEY RESOURCES TABLE**
- **RESOURCE AVAILABILITY**
 - Lead contact
 - Materials availability
 - Data and code availability
- **EXPERIMENTAL MODEL AND SUBJECT DETAILS**
 - Human subjects
 - Human oocytes
 - Human embryos
 - Sperm donation and processing
 - Murine oocytes
- **METHOD DETAILS**
 - Embryo culture and Drug incubations
 - Cas9 RNP preparation and injection
 - Artificial activation
 - Immunocytochemistry of Human and Murine Embryos
 - DNA fiber analysis
 - Confocal microscopy and DNA damage foci analysis
 - Single-cell/single nuclei whole genome amplification and sequencing
 - Single-cell / single-nuclei sequencing analysis and copy number inference
 - Break site annotations
- **QUANTIFICATION AND STATISTICAL ANALYSIS**
 - Analysis of DNA damage and embryo development

SUPPLEMENTAL INFORMATION

Supplemental information can be found online at <https://doi.org/10.1016/j.cell.2022.06.028>.

ACKNOWLEDGMENTS

We thank anonymous gamete and embryo donors. We thank Egli lab members and the members of Columbia University Fertility Center (CUFC) for their valuable input to the work. We thank Kevin Lambrese (Sincera Reproductive Medicine) for help with the procurement of embryos, Zev Williams and Eric Forman (CUFC) for help with the oocyte and embryo donations, Gist Croft (NYSCF-RI) for confocal imaging help, Christine Lin for graphical help, and Sara Goodwin (CSHL) for next-generation sequencing. This research was supported by the NYSCF-Robertson Stem Cell Investigator award, NYSTEM grants #C32564GG, the US Israel Binational Science Foundation grant # 2015089, a Columbia Stem Cell Initiative Seed grant, the ASRM award CU16-1576, the John M. Driscoll Jr. Children's Fund Scholarship, and by the Russell Berrie Foundation Program in Cellular Therapies. K.L.P., S.A. J.d.P., A.R., and J.T. were supported by a clinical fellowship in reproductive endocrinology and infertility. T.B. is supported by the William C. and Joyce C. O'Neil Charitable Trust, MSK Single-Cell Sequencing Initiative.

AUTHOR CONTRIBUTIONS

K.L.P., S.A., and A.D.L.A. designed the studies. K.L.P. performed the immunostaining, confocal microscopy, foci quantification, and developmental analysis with contributions from J.d.P. and M.V.Z. A.R. assisted with embryo thaws; J.T. designed the gRNA. A.D.L.A., S.A., and S.X. performed the single-cell amplification and library preparation. S.X. and A.S. performed the analysis of the gene expression data. S.X. and T.B. performed the copy-number analysis with contribution from D.J.M. and A.K.; T.B. provided expertise and reagents on single-cell amplification. S.A., A.D.L.A., and S.X. performed the break-point mapping. K.L.P., S.A., A.D.L.A., S.X., and N.W. interpreted the results. R.L. recruited oocyte donors; R.L., K.L.P., and S.A. performed oocyte retrievals; B.P. processed oocytes. N.W. performed the DNA fiber analysis. A.T. performed the irradiation. A.C. and A.T. provided data interpretation. K.L.P., S.A., and A.D.L.A. wrote the paper with input from all authors. D.E. contributed to all aspects.

DECLARATION OF INTERESTS

D.E. is a member of the *Cell* editorial board.

Received: April 4, 2021

Revised: September 3, 2021

Accepted: June 15, 2022

Published: July 19, 2022

REFERENCES

- Aguilar, J., Motato, Y., Escribá, M.J., Ojeda, M., Muñoz, E., and Meseguer, M. (2014). The human first cell cycle: impact on implantation. *Reprod. Biomed. Online* 28, 475–484.
- Ahuja, A.K., Jodkowska, K., Teloni, F., Bizard, A.H., Zellweger, R., Herrador, R., Ortega, S., Hickson, I.D., Altmeyer, M., Mendez, J., and Lopes, M. (2016). A short G1 phase imposes constitutive replication stress and fork remodelling in mouse embryonic stem cells. *Nat. Commun.* 7, 10660.
- Anantha, R.W., Vassin, V.M., and Borowiec, J.A. (2007). Sequential and synergistic modification of human RPA stimulates chromosomal DNA repair. *J. Biol. Chem.* 282, 35910–35923.
- Babariya, D., Fragouli, E., Alfarawati, S., Spath, K., and Wells, D. (2017). The incidence and origin of segmental aneuploidy in human oocytes and preimplantation embryos. *Hum. Reprod.* 32, 2549–2560.
- Baslan, T., Kendall, J., Rodgers, L., Cox, H., Riggs, M., Stepansky, A., Troge, J., Ravi, K., Esposito, D., Lakshmi, B., et al. (2012). Genome-wide copy number analysis of single cells. *Nat. Protoc.* 7, 1024–1041.
- Baslan, T., Kendall, J., Ward, B., Cox, H., Leotta, A., Rodgers, L., Riggs, M., D'italia, S., Sun, G., Yong, M., et al. (2015). Optimizing sparse sequencing of single cells for highly multiplex copy number profiling. *Genome Res.* 25, 714–724.
- Bester, A.C., Roniger, M., Oren, Y.S., Im, M.M., Sarni, D., Chaoat, M., Bensimon, A., Zamir, G., Shewach, D.S., and Kerem, B. (2011). Nucleotide deficiency promotes genomic instability in early stages of cancer development. *Cell* 145, 435–446.
- Bohgaki, T., Bohgaki, M., Cardoso, R., Panier, S., Zeegers, D., Li, L., Stewart, G.S., Sanchez, O., Hande, M.P., Durocher, D., et al. (2011). Genomic instability, defective spermatogenesis, immunodeficiency, and cancer in a mouse model of the RIDDLE syndrome. *PLOS Genet* 7, e1001381.
- Bolton, H., Graham, S.J.L., Van Der Aa, N., Kumar, P., Theunis, K., Fernandez Gallardo, E., Voet, T., and Zernicka-Goetz, M. (2016). Mouse model of chromosome mosaicism reveals lineage-specific depletion of aneuploid cells and normal developmental potential. *Nat. Commun.* 7, 11165.
- Braude, P., Bolton, V., and Moore, S. (1988). Human gene expression first occurs between the four- and eight-cell stages of preimplantation development. *Nature* 332, 459–461.
- Brisson, O., El-Hilali, S., Azar, D., Koundrioukoff, S., Schmidt, M., Nähse, V., Jaszczyszyn, Y., Lachages, A.M., Dutrillaux, B., Thernes, C., et al. (2019).

Transcription-mediated organization of the replication initiation program across large genes sets common fragile sites genome-wide. *Nat. Commun.* **10**, 5693.

Bui, H.T., Wakayama, S., Kishigami, S., Park, K.K., Kim, J.H., Thuan, N.V., and Wakayama, T. (2010). Effect of trichostatin A on chromatin remodeling, histone modifications, DNA replication, and transcriptional activity in cloned mouse embryos. *Biol. Reprod.* **83**, 454–463.

Burrell, R.A., McClelland, S.E., Endesfelder, D., Groth, P., Weller, M.C., Shaikh, N., Domingo, E., Kanu, N., Dewhurst, S.M., Gronroos, E., et al. (2013). Replication stress links structural and numerical cancer chromosomal instability. *Nature* **494**, 492–496.

Cavazza, T., Takeda, Y., Politi, A.Z., Aushev, M., Aldag, P., Baker, C., Choudhary, M., Bucevičius, J., Lukinavičius, G., Elder, K., et al. (2021). Parental genome unification is highly error-prone in mammalian embryos. *Cell* **184**, 2860–2877. e22.

Chang, B.H., Smith, L., Huang, J., and Thayer, M. (2007). Chromosomes with delayed replication timing lead to checkpoint activation, delayed recruitment of Aurora B and chromosome instability. *Oncogene* **26**, 1852–1861.

Charrier, J.D., Durrant, S.J., Golec, J.M., Kay, D.P., Knechtel, R.M., McCormick, S., Mortimore, M., O'Donnell, M.E., Pinder, J.L., Reaper, P.M., et al. (2011). Discovery of potent and selective inhibitors of ataxia telangiectasia mutated and Rad3 related (ATR) protein kinase as potential anticancer agents. *J. Med. Chem.* **54**, 2320–2330.

Chavez, S.L., Loewke, K.E., Han, J., Moussavi, F., Colls, P., Munne, S., Behr, B., and Reijo Pera, R.A. (2012). Dynamic blastomere behaviour reflects human embryo ploidy by the four-cell stage. *Nat. Commun.* **3**, 1251.

Cheng, X., Yang, Q., Liu, J., Ye, J., Xiao, H., Zhang, G., Pan, Y., Li, X., Hao, R., and Li, Y. (2019). Constitutional 763.3 Kb chromosome 1q43 duplication encompassing only CHRM3 gene identified by next generation sequencing (NGS) in a child with intellectual disability. *Mol. Cytogenet.* **12**, 16.

Chia, G., Agudo, J., Treff, N., Sauer, M.V., Billing, D., Brown, B.D., Baer, R., and Egli, D. (2017). Genomic instability during reprogramming by nuclear transfer is DNA replication dependent. *Nat. Cell Biol.* **19**, 282–291.

Coorens, T.H.H., Oliver, T.R.W., Sanghvi, R., Sovio, U., Cook, E., Vento-Tormo, R., Haniffa, M., Young, M.D., Rahbari, R., Sebire, N., et al. (2021). Inherent mosaicism and extensive mutation of human placentas. *Nature* **592**, 80–85.

Coticchio, G., Mignini Renzini, M., Novara, P.V., Lain, M., De Ponti, E., Turchi, D., Fadini, R., and Dal Canto, M. (2018). Focused time-lapse analysis reveals novel aspects of human fertilization and suggests new parameters of embryo viability. *Hum. Reprod.* **33**, 23–31.

Crasta, K., Ganem, N.J., Dagher, R., Lantermann, A.B., Ivanova, E.V., Pan, Y., Nezi, L., Protopopov, A., Chowdhury, D., and Pellman, D. (2012). DNA breaks and chromosome pulverization from errors in mitosis. *Nature* **482**, 53–58.

Danecek, P., Bonfield, J.K., Liddle, J., Marshall, J., Ohan, V., Pollard, M.O., Whitwham, A., Keane, T., McCarthy, S.A., Davies, R.M., and Li, H. (2021). Twelve years of SAMtools and BCFtools. *GigaScience* **10**.

Daphnis, D.D., Fragouli, E., Economou, K., Jerkovic, S., Craft, I.L., Delhanty, J.D., and Harper, J.C. (2008). Analysis of the evolution of chromosome abnormalities in human embryos from Day 3 to 5 using CGH and FISH. *Mol. Hum. Reprod.* **14**, 117–125.

Doil, C., Mailland, N., Bekker-Jensen, S., Menard, P., Larsen, D.H., Pepperkok, R., Ellenberg, J., Panier, S., Durocher, D., Bartek, J., et al. (2009). RNF168 binds and amplifies ubiquitin conjugates on damaged chromosomes to allow accumulation of repair proteins. *Cell* **136**, 435–446.

Duda, H., Arter, M., Gloggnitzer, J., Teloni, F., Wild, P., Blanco, M.G., Altmeyer, M., and Matos, J. (2016). A mechanism for controlled breakage of under-replicated chromosomes during mitosis. *Dev. Cell* **39**, 740–755.

Dupré, A., Boyer-Chatenet, L., Sattler, R.M., Modi, A.P., Lee, J.H., Nicolette, M.L., Kopelovich, L., Jasin, M., Baer, R., Paull, T.T., and Gautier, J. (2008). A forward chemical genetic screen reveals an inhibitor of the Mre11-Rad50-Nbs1 complex. *Nat. Chem. Biol.* **4**, 119–125.

Egeli, D., Chen, A.E., Saphier, G., Ichida, J., Fitzgerald, C., Go, K.J., Acevedo, N., Patel, J., Baetscher, M., Kearns, W.G., et al. (2011). Reprogramming within

hours following nuclear transfer into mouse but not human zygotes. *Nat. Commun.* **2**, 488.

Ercilla, A., Benada, J., Amitash, S., Zonderland, G., Baldi, G., Somyajit, K., Ochs, F., Costanzo, V., Lukas, J., and Toledo, L. (2020). Physiological tolerance to ssDNA enables strand uncoupling during DNA replication. *Cell Rep.* **30**, 2416–2429. e7.

Escribà, M.J., Vendrell, X., and Peinado, V. (2019). Segmental aneuploidy in human blastocysts: a qualitative and quantitative overview. *Reprod. Biol. Endocrinol.* **17**, 76.

Feng, W., and Jasin, M. (2017). BRCA2 suppresses replication stress-induced mitotic and G1 abnormalities through homologous recombination. *Nat. Commun.* **8**, 525.

Fenwick, J., Platteau, P., Murdoch, A.P., and Herbert, M. (2002). Time from insemination to first cleavage predicts developmental competence of human preimplantation embryos in vitro. *Hum. Reprod.* **17**, 407–412.

Franasiak, J.M., Forman, E.J., Hong, K.H., Werner, M.D., Upham, K.M., Treff, N.R., and Scott, R.T., Jr. (2014). The nature of aneuploidy with increasing age of the female partner: a review of 15, 169 consecutive trophoctoderm biopsies evaluated with comprehensive chromosomal screening. *Fertil. Steril.* **101**, 656–663.e1.

Gimelli, S., Capra, V., Di Rocco, M., Leoni, M., Mirabelli-Badenier, M., Schiaffino, M.C., Fiorio, P., Cuoco, C., Gimelli, G., and Tassano, E. (2014). Interstitial 7q31.1 copy number variations disrupting IMMP2L gene are associated with a wide spectrum of neurodevelopmental disorders. *Mol. Cytogenet.* **7**, 54.

Girardi, L., Serdarogullari, M., Patassini, C., Poli, M., Fabiani, M., Caroselli, S., Coban, O., Findikli, N., Boynukalin, F.K., Bahceci, M., et al. (2020). Incidence, origin, and predictive model for the detection and clinical management of segmental aneuploidies in human embryos. *Am. J. Hum. Genet.* **106**, 525–534.

Gruhn, J.R., Zielinska, A.P., Shukla, V., Blanshard, R., Capalbo, A., Cima-domo, D., Nikiforov, D., Chan, A.C., Newnham, L.J., Vogel, I., et al. (2019). Chromosome errors in human eggs shape natural fertility over reproductive life span. *Science* **365**, 1466–1469.

Guo, H., Zhu, P., Yan, L., Li, R., Hu, B., Lian, Y., Yan, J., Ren, X., Lin, S., Li, J., et al. (2014). The DNA methylation landscape of human early embryos. *Nature* **511**, 606–610.

Hamperl, S., Bocek, M.J., Saldívar, J.C., Swigut, T., and Cimprich, K.A. (2017). Transcription-replication conflict orientation modulates R-loop levels and activates distinct DNA damage responses. *Cell* **170**, 774–786. e19.

Harrigan, J.A., Belotserkovskaya, R., Coates, J., Dimitrova, D.S., Polo, S.E., Bradshaw, C.R., Fraser, P., and Jackson, S.P. (2011). Replication stress induces 53BP1-containing OPT domains in G1 cells. *J. Cell Biol.* **193**, 97–108.

Helmrich, A., Ballarino, M., and Tora, L. (2011). Collisions between replication and transcription complexes cause common fragile site instability at the longest human genes. *Mol. Cell* **44**, 966–977.

Hirai, H., Iwasawa, Y., Okada, M., Arai, T., Nishibata, T., Kobayashi, M., Kimura, T., Kaneko, N., Ohtani, J., Yamanaka, K., et al. (2009). Small-molecule inhibition of Wee1 kinase by MK-1775 selectively sensitizes p53-deficient tumor cells to DNA-damaging agents. *Mol. Cancer Ther.* **8**, 2992–3000.

Hook, E.B., and Warburton, D. (1983). The distribution of chromosomal genotypes associated with Turner's syndrome: livebirth prevalence rates and evidence for diminished fetal mortality and severity in genotypes associated with structural X abnormalities or mosaicism. *Hum. Genet.* **64**, 24–27.

Ikegami, S., Taguchi, T., Ohashi, M., Oguro, M., Nagano, H., and Mano, Y. (1978). Aphidicolin prevents mitotic cell division by interfering with the activity of DNA polymerase-alpha. *Nature* **275**, 458–460.

Iyer, D.R., and Rhind, N. (2017). Replication fork slowing and stalling are distinct, checkpoint-independent consequences of replicating damaged DNA. *PLoS Genet.* **13**, e1006958.

Jackson, D.A., and Pombo, A. (1998). Replicon clusters are stable units of chromosome structure: evidence that nuclear organization contributes to the

- efficient activation and propagation of S phase in human cells. *J. Cell Biol.* **140**, 1285–1295.
- Ji, F., Liao, H., Pan, S., Ouyang, L., Jia, F., Fu, Z., Zhang, F., Geng, X., Wang, X., Li, T., et al. (2020). Genome-wide high-resolution mapping of mitotic DNA synthesis sites and common fragile sites by direct sequencing. *Cell Res.* **30**, 1009–1023.
- Joseph, S.A., Tagliatalata, A., Leuzzi, G., Huang, J.W., Cuella-Martin, R., and Ciccio, A. (2020). Time for remodeling: SNF2-family DNA translocases in replication fork metabolism and human disease. *DNA Repair (Amst)* **95**, 102943.
- Ju, Y.S., Martincorena, I., Gerstung, M., Petljak, M., Alexandrov, L.B., Rahbari, R., Wedge, D.C., Davies, H.R., Ramakrishna, M., Fullam, A., et al. (2017). Somatic mutations reveal asymmetric cellular dynamics in the early human embryo. *Nature* **543**, 714–718.
- Kiessling, A.A., Bletsas, R., Desmarais, B., Mara, C., Kallianidis, K., and Loutradis, D. (2010). Genome-wide microarray evidence that 8-cell human blastomeres over-express cell cycle drivers and under-express checkpoints. *J. Assist. Reprod. Genet.* **27**, 265–276.
- King, C., Diaz, H., Barnard, D., Barda, D., Clawson, D., Blosser, W., Cox, K., Guo, S., and Marshall, M. (2014). Characterization and preclinical development of LY2603618: a selective and potent Chk1 inhibitor. *Invest. New Drugs* **32**, 213–226.
- Kuo, L.J., and Yang, L.X. (2008). Gamma-H2AX—a novel biomarker for DNA double-strand breaks. *Vivo* **22**, 305–309.
- Larsson, A.J.M., Stanley, G., Sinha, R., Weissman, I.L., and Sandberg, R. (2018). Computational correction of index switching in multiplexed sequencing libraries. *Nat. Methods* **15**, 305–307.
- Le Beau, M.M., Rassool, F.V., Neilly, M.E., Espinosa, R., 3rd, Glover, T.W., Smith, D.I., and Mckeithan, T.W. (1998). Replication of a common fragile site, FRA3B, occurs late in S phase and is delayed further upon induction: implications for the mechanism of fragile site induction. *Hum. Mol. Genetics* **7**, 755–761.
- Lee, M.J., Lee, R.K., Lin, M.H., and Hwu, Y.M. (2012). Cleavage speed and implantation potential of early-cleavage embryos in IVF or ICSI cycles. *J. Assist. Reprod. Genet.* **29**, 745–750.
- Letessier, A., Millot, G.A., Koundrioukoff, S., Lachagès, A.M., Vogt, N., Hansen, R.S., Malfoy, B., Brison, O., and Debatisse, M. (2011). Cell-type-specific replication initiation programs set fragility of the FRA3B fragile site. *Nature* **470**, 120–123.
- Li, H., and Durbin, R. (2009). Fast and accurate short read alignment with Burrows-Wheeler transform. *Bioinformatics* **25**, 1754–1760.
- Liaw, H., Lee, D., and Myung, K. (2011). DNA-PK-dependent RPA2 hyperphosphorylation facilitates DNA repair and suppresses sister chromatid exchange. *PLoS One* **6**, e21424.
- Liu, Q., Guntuku, S., Cui, X.S., Matsuoka, S., Cortez, D., Tamai, K., Luo, G., Carattini-Rivera, S., Demayo, F., Bradley, A., et al. (2000). Chk1 is an essential kinase that is regulated by Atr and required for the G(2)/M DNA damage checkpoint. *Genes Dev* **14**, 1448–1459.
- Liu, S., Opiyo, S.O., Manthey, K., Glanzer, J.G., Ashley, A.K., Amerin, C., Troksa, K., Shrivastav, M., Nickloff, J.A., and Oakley, G.G. (2012). Distinct roles for DNA-PK, ATM and ATR in RPA phosphorylation and checkpoint activation in response to replication stress. *Nucleic Acids Res.* **40**, 10780–10794.
- Lukas, C., Savic, V., Bekker-Jensen, S., Doil, C., Neumann, B., Pedersen, R.S., Grøfte, M., Chan, K.L., Hickson, I.D., Bartek, J., and Lukas, J. (2011). 53BP1 nuclear bodies form around DNA lesions generated by mitotic transmission of chromosomes under replication stress. *Nat. Cell Biol.* **13**, 243–253.
- Macheret, M., Bhowmick, R., Sobkowiak, K., Padayachy, L., Mailler, J., Hickson, I.D., and Halazonetis, T.D. (2020). High-resolution mapping of mitotic DNA synthesis regions and common fragile sites in the human genome through direct sequencing. *Cell Res* **30**, 997–1008.
- Mankouri, H.W., Huttner, D., and Hickson, I.D. (2013). How unfinished business from S-phase affects mitosis and beyond. *EMBO J.* **32**, 2661–2671.
- Maya-Mendoza, A., Moudry, P., Merchut-Maya, J.M., Lee, M., Strauss, R., and Bartek, J. (2018). High speed of fork progression induces DNA replication stress and genomic instability. *Nature* **559**, 279–284.
- Mocanu, C., Karanika, E., Fernández-Casañas, M., Herbert, A., Olukoga, T., Özgürsüs, M.E., and Chan, K.L. (2022). DNA replication is highly resilient and persistent under the challenge of mild replication stress. *Cell Rep.* **39**, 110701.
- Moreno, A., Carrington, J.T., Albergante, L., Al Mamun, M., Haagen, E.J., Komseli, E.S., Gorgoulis, V.G., Newman, T.J., and Blow, J.J. (2016). Unreplicated DNA remaining from unperturbed S phases passes through mitosis for resolution in daughter cells. *Proc. Natl. Acad. Sci. USA* **113**, E5757–E5764.
- Mrasek, K., Schoder, C., Teichmann, A.C., Behr, K., Franze, B., Wilhelm, K., Blaurock, N., Claussen, U., Liehr, T., and Weise, A. (2010). Global screening and extended nomenclature for 230 aphidicolin-inducible fragile sites, including 61 yet unreported ones. *Int. J. Oncol.* **36**, 929–940.
- Nakatani, T., Lin, J., Ji, F., Ettinger, A., Pontabry, J., Tokoro, M., Altamirano-Pacheco, L., Fiorentino, J., Mahammadov, E., Hatano, Y., et al. (2022). DNA replication fork speed underlies cell fate changes and promotes reprogramming. *Nat. Genet.* **54**, 318–327.
- Navin, N., Kendall, J., Troge, J., Andrews, P., Rodgers, L., Mcindoo, J., Cook, K., Stepansky, A., Levy, D., Esposito, D., et al. (2011). Tumour evolution inferred by single-cell sequencing. *Nature* **472**, 90–94.
- Olshen, A.B., Venkatraman, E.S., Lucito, R., and Wigler, M. (2004). Circular binary segmentation for the analysis of array-based DNA copy number data. *Biostatistics* **5**, 557–572.
- Orlando, L., Tanasijevic, B., Nakanishi, M., Reid, J.C., García-Rodríguez, J.L., Chauhan, K.D., Porras, D.P., Aslostovar, L., Lu, J.D., Shapovalova, Z., et al. (2021). Phosphorylation state of the histone variant H2A.X controls human stem and progenitor cell fate decisions. *Cell Rep* **34**, 108818.
- Ottolini, C.S., Kitchen, J., Xanthopoulou, L., Gordon, T., Summers, M.C., and Handyside, A.H. (2017). Tripolar mitosis and partitioning of the genome arrests human preimplantation development in vitro. *Sci Rep. Sci. Rep.* **7**, 9744.
- Palmerola, K.L., Rudick, B.J., and Lobo, R.A. (2018). Low estradiol responses in oocyte donors undergoing gonadotropin stimulation do not influence clinical outcomes. *J. Assist. Reprod. Genet.* **35**, 1675–1682.
- Perrone, M.D., Rocca, M.S., Bruno, I., Faletta, F., Pecile, V., and Gasparini, P. (2012). De novo 911 Kb interstitial deletion on chromosome 1q43 in a boy with mental retardation and short stature. *Eur. J. Med. Genet.* **55**, 117–119.
- Pertea, M., Shumate, A., Pertea, G., Varabyou, A., Chang, Y.-C., Madugundu, A.K., Pandey, A., and Salzberg, S.L. (2018). Thousands of large-scale RNA sequencing experiments yield a comprehensive new human gene list and reveal extensive transcriptional noise. *bioRxiv*. 10.1101/332825.
- Petermann, E., Orta, M.L., Issaeva, N., Schultz, N., and Helleday, T. (2010). Hydroxyurea-stalled replication forks become progressively inactivated and require two different RAD51-mediated pathways for restart and repair. *Mol. Cell* **37**, 492–502.
- Piberger, A.L., Bowry, A., Kelly, R.D.W., Walker, A.K., González-Acosta, D., Bailey, L.J., Doherty, A.J., Méndez, J., Morris, J.R., Bryant, H.E., and Petermann, E. (2020). PrimPol-dependent single-stranded gap formation mediates homologous recombination at bulky DNA adducts. *Nat. Commun.* **11**, 5863.
- Quinlan, A.R., and Hall, I.M. (2010). BEDTools: a flexible suite of utilities for comparing genomic features. *Bioinformatics* **26**, 841–842.
- Racowsky, C., Vernon, M., Mayer, J., Ball, G.D., Behr, B., Pomeroy, K.O., Winer, D., Gibbons, W., Conaghan, J., and Stern, J.E. (2010). Standardization of grading embryo morphology. *Fertil. Steril.* **94**, 1152–1153.
- Raderschall, E., Golub, E.I., and Haaf, T. (1999). Nuclear foci of mammalian recombination proteins are located at single-stranded DNA regions formed after DNA damage. *Proc. Natl. Acad. Sci. USA* **96**, 1921–1926.
- Richardson, A., Brearley, S., Ahitan, S., Chamberlain, S., Davey, T., Zujovic, L., Hopkisson, J., Campbell, B., and Raine-Fenning, N. (2015). A clinically useful simplified blastocyst grading system. *Reprod. Biomed. Online* **31**, 523–530.
- Rodin, R.E., Dou, Y., Kwon, M., Sherman, M.A., D’Gama, A.M., Doan, R.N., Rento, L.M., Girsakis, K.M., Bohrsen, C.L., Kim, S.N., et al. (2021). The landscape of somatic mutation in cerebral cortex of autistic and neurotypical

- individuals revealed by ultra-deep whole-genome sequencing. *Nat. Neurosci.* **24**, 176–185.
- Sakkas, D., Shoukir, Y., Chardonnes, D., Bianchi, P.G., and Campana, A. (1998). Early cleavage of human embryos to the two-cell stage after intracytoplasmic sperm injection as an indicator of embryo viability. *Hum. Reprod.* **13**, 182–187.
- Sarni, D., Sasaki, T., Irony Tur-Sinai, M., Miron, K., Rivera-Mulia, J.C., Magnusson, B., Ljungman, M., Gilbert, D.M., and Kerem, B. (2020). 3D genome organization contributes to genome instability at fragile sites. *Nat. Commun.* **11**, 3613.
- Scheinin, I., Sie, D., Bengtsson, H., Van De Wiel, M.A., Olshen, A.B., Van Thuijl, H.F., Van Essen, H.F., Eijk, P.P., Rustenburg, F., Meijer, G.A., et al. (2014). DNA copy number analysis of fresh and formalin-fixed specimens by shallow whole-genome sequencing with identification and exclusion of problematic regions in the genome assembly. *Genome Res.* **24**, 2022–2032.
- Schultz, L.B., Chehab, N.H., Malikzay, A., and Halazonetis, T.D. (2000). p53 binding protein 1 (53BP1) is an early participant in the cellular response to DNA double-strand breaks. *J. Cell Biol.* **151**, 1381–1390.
- Shapiro, B.S., Harris, D.C., and Richter, K.S. (2000). Predictive value of 72-hour blastomere cell number on blastocyst development and success of subsequent transfer based on the degree of blastocyst development. *Fertil. Steril.* **73**, 582–586.
- Shibata, A., Conrad, S., Birraux, J., Geuting, V., Barton, O., Ismail, A., Kakarougkas, A., Meek, K., Taucher-Scholz, G., Löbrich, M., and Jeggo, P.A. (2011). Factors determining DNA double-strand break repair pathway choice in G2 phase. *EMBO J.* **30**, 1079–1092.
- Shibata, A., Moiani, D., Arvai, A.S., Perry, J., Harding, S.M., Genois, M.M., Maity, R., Van Rossum-Fikkert, S., Kertokallio, A., Romoli, F., et al. (2014). DNA double-strand break repair pathway choice is directed by distinct MRE11 nuclease activities. *Mol. Cell* **53**, 7–18.
- Shimajima, K., Okamoto, N., and Yamamoto, T. (2017). Possible genes responsible for developmental delay observed in patients with rare 2q23q24 microdeletion syndrome: literature review and description of an additional patient. *Congenit. Anom. (Kyoto)* **57**, 109–113.
- Simon, L., Lutton, D., Mcmanus, J., and Lewis, S.E.M. (2011). Sperm DNA damage measured by the alkaline Comet assay as an independent predictor of male infertility and in vitro fertilization success. *Fertil. Steril.* **95**, 652–657.
- Tachibana, M., Amato, P., Sparman, M., Gutierrez, N.M., Tippner-Hedges, R., Ma, H., Kang, E., Fulati, A., Lee, H.S., Sritanandomchai, H., et al. (2013). Human embryonic stem cells derived by somatic cell nuclear transfer. *Cell* **153**, 1228–1238.
- Tercero, J.A., and Diffley, J.F.X. (2001). Regulation of DNA replication fork progression through damaged DNA by the Mec1/Rad53 checkpoint. *Nature* **412**, 553–557.
- Thompson, P.S., and Cortez, D. (2020). New insights into abasic site repair and tolerance. *DNA Repair* **90**, 102866.
- Turocy, J., Marin, D., Xu, S., Xu, J., Robles, A., Treff, N., and Egli, D. (2022). DNA double strand breaks cause chromosome loss through sister chromatid tethering in human embryos. *bioRxiv*. 2022.03.10.483502. <https://doi.org/10.1101/2022.03.10.483502>.
- Van Bever, Y., Rooms, L., Laridon, A., Reyniers, E., Van Luijk, R., Scheers, S., Wauters, J., and Kooy, R.F. (2005). Clinical report of a pure subtelomeric 1qter deletion in a boy with mental retardation and multiple anomalies adds further evidence for a specific phenotype. *Am. J. Med. Genet. A* **135**, 91–95.
- Van Montfoort, A.P., Dumoulin, J.C., Kester, A.D., and Evers, J.L. (2004). Early cleavage is a valuable addition to existing embryo selection parameters: a study using single embryo transfers. *Hum. Reprod.* **19**, 2103–2108.
- Vanneste, E., Voet, T., Le Caignec, C., Ampe, M., Konings, P., Melotte, C., Debrock, S., Amyere, M., Viikkula, M., Schuit, F., et al. (2009). Chromosome instability is common in human cleavage-stage embryos. *Nat. Med.* **15**, 577–583.
- Vassin, V.M., Anantha, R.W., Sokolova, E., Kanner, S., and Borowiec, J.A. (2009). Human RPA phosphorylation by ATR stimulates DNA synthesis and prevents ssDNA accumulation during DNA-replication stress. *J. Cell Sci.* **122**, 4070–4080.
- Vera-Rodriguez, M., Chavez, S.L., Rubio, C., Reijo Pera, R.A., and Simon, C. (2015). Prediction model for aneuploidy in early human embryo development revealed by single-cell analysis. *Nat. Commun.* **6**, 7601.
- Wang, M., Wei, P.C., Lim, C.K., Gallina, I.S., Marshall, S., Marchetto, M.C., Alt, F.W., and Gage, F.H. (2020). Increased neural progenitor proliferation in a hiPSC model of autism induces replication stress-associated genome instability. *Cell Stem Cell* **26**, 221–233. e6.
- Wang, X.W., Zhan, Q., Coursen, J.D., Khan, M.A., Kontny, H.U., Yu, L., Hollander, M.C., O'Connor, P.M., Fornace, A.J., Jr., and Harris, C.C. (1999). GADD45 induction of a G2/M cell cycle checkpoint. *Proc. Natl. Acad. Sci. USA* **96**, 3706–3711.
- Ward, I.M., and Chen, J. (2001). Histone H2AX is phosphorylated in an ATR-dependent manner in response to replicational stress. *J. Biol. Chem.* **276**, 47759–47762.
- Wei, P.C., Chang, A.N., Kao, J., Du, Z., Meyers, R.M., Alt, F.W., and Schwer, B. (2016). Long neural genes harbor recurrent DNA break clusters in neural stem/progenitor cells. *Cell* **164**, 644–655.
- Widrow, R.J., Hansen, R.S., Kawame, H., Gartler, S.M., and Laird, C.D. (1998). Very late DNA replication in the human cell cycle. *Proc. Natl. Acad. Sci. USA* **95**, 11246–11250.
- Wilhelm, T., Magdalou, I., Barascu, A., Técher, H., Debatisse, M., and Lopez, B.S. (2014). Spontaneous slow replication fork progression elicits mitosis alterations in homologous recombination-deficient mammalian cells. *Proc. Natl. Acad. Sci. USA* **111**, 763–768.
- Wilson, T.E., Arlt, M.F., Park, S.H., Rajendran, S., Paulsen, M., Ljungman, M., and Glover, T.W. (2015). Large transcription units unify copy number variants and common fragile sites arising under replication stress. *Genome Res.* **25**, 189–200.
- Wong, C.C., Loewke, K.E., Bossert, N.L., Behr, B., De Jonge, C.J., Baer, T.M., and Reijo Pera, R.A. (2010). Non-invasive imaging of human embryos before embryonic genome activation predicts development to the blastocyst stage. *Nat. Biotechnol.* **28**, 1115–1121.
- Wossidlo, M., Arand, J., Sebastiano, V., Lepikhov, K., Boiani, M., Reinhardt, R., Schöler, H., and Walter, J. (2010). Dynamic link of DNA demethylation, DNA strand breaks and repair in mouse zygotes. *EMBO J.* **29**, 1877–1888.
- Wright, G.E., Hübscher, U., Khan, N.N., Focher, F., and Verri, A. (1994). Inhibitor analysis of calf thymus DNA polymerases alpha, delta and epsilon. *FEBS Lett* **341**, 128–130.
- Xie, D., Chen, C.C., Ptaszek, L.M., Xiao, S., Cao, X., Fang, F., Ng, H.H., Lewin, H.A., Cowan, C., and Zhong, S. (2010). Rewirable gene regulatory networks in the preimplantation embryonic development of three mammalian species. *Genome Res.* **20**, 804–815.
- Xue, Z., Huang, K., Cai, C., Cai, L., Jiang, C.Y., Feng, Y., Liu, Z., Zeng, Q., Cheng, L., Sun, Y.E., et al. (2013). Genetic programs in human and mouse early embryos revealed by single-cell RNA sequencing. *Nature* **500**, 593–597.
- Yamada, M., and Egli, D. (2017). Genome transfer prevents fragmentation and restores developmental potential of developmentally compromised postovulatory aged mouse oocytes. *Stem Cell Rep.* **8**, 576–588.
- Yan, L., Yang, M., Guo, H., Yang, L., Wu, J., Li, R., Liu, P., Lian, Y., Zheng, X., Yan, J., et al. (2013). Single-cell RNA-Seq profiling of human preimplantation embryos and embryonic stem cells. *Nat. Struct. Mol. Biol.* **20**, 1131–1139.
- Zabludoff, S.D., Deng, C., Grondine, M.R., Sheehy, A.M., Ashwell, S., Cable, B.L., Green, S., Haye, H.R., Horn, C.L., Janetka, J.W., et al. (2008). AZD7762, a novel checkpoint kinase inhibitor, drives checkpoint abrogation and potentiates DNA-targeted therapies. *Mol. Cancer Ther.* **7**, 2955–2966.
- Zakarin Safier, L., Gumer, A., Kline, M., Egli, D., and Sauer, M.V. (2018). Compensating human subjects providing oocytes for stem cell research: 9-year experience and outcomes. *J. Assist. Reprod. Genet.* **35**, 1219–1225.

- Zellweger, R., Dalcher, D., Mutreja, K., Berti, M., Schmid, J.A., Herrador, R., Vindigni, A., and Lopes, M. (2015). Rad51-mediated replication fork reversal is a global response to genotoxic treatments in human cells. *J. Cell Biol.* *208*, 563–579.
- Zhou, S., Cheng, D., Ouyang, Q., Xie, P., Lu, C., Gong, F., Hu, L., Tan, Y., Lu, G., and Lin, G. (2018). Prevalence and authenticity of de-novo segmental aneuploidy (>16 Mb) in human blastocysts as detected by next-generation sequencing. *Reprod. Biomed. Online* *37*, 511–520.
- Zou, L., and Elledge, S.J. (2003). Sensing DNA damage through ATRIP recognition of RPA-ssDNA complexes. *Science* *300*, 1542–1548.
- Zuazua-Villar, P., Ganesh, A., Phear, G., Gagou, M.E., and Meuth, M. (2015). Extensive RPA2 hyperphosphorylation promotes apoptosis in response to DNA replication stress in CHK1 inhibited cells. *Nucleic Acids Res.* *43*, 9776–9787.
- Zuccaro, M.V., Xu, J., Mitchell, C., Marin, D., Zimmerman, R., Rana, B., Weinstein, E., King, R.T., Palmerola, K.L., Smith, M.E., et al. (2020). Allele-specific chromosome removal after Cas9 cleavage in human embryos. *Cell* *183*, 1650–1664. e15.

STAR★METHODS

KEY RESOURCES TABLE

REAGENT or RESOURCE	SOURCE	IDENTIFIER
Antibodies		
Anti-phospho-Histone H2A.X-Ser139 mouse monoclonal Ab. Does not react to S139A in human pluripotent stem cells (Orlando et al., 2021). Figure S4C shows ATR dependent phosphorylation.	Millipore	Cat# 05-636; RRID:AB_309864
Phospho-Chk1 (Ser317) (D12H3) XP Rabbit mAb; according to the manufacturer, this monoclonal antibody does not recognize CHK1 after dephosphorylation with CIP, and shows increased signal after UV treatment. Figure S11 shows ATR dependent phosphorylation in mouse embryos.	Cell Signaling Technology	Cat# 12302S; RRID:AB_2783865
anti 53BP1 (rabbit polyclonal, used in mice)	Novus Biologicals	Cat# NB100-904
Purified mouse anti human 53BP1, clone 19	BD Transduction laboratories	Cat# 612522; RRID:AB_2206766
Rpa32/rpa2 (4E4) Rat monoclonal Ab	Cell Signaling Technology	Cat# 2208S; RRID:AB_2238543
Anti-Rad51 (Ab-1) Rabbit pAb. Figure S4C shows ATR dependent foci formation	EMD Millipore	Cat# PC130; lot #D00 138544
Centromere protein antibody (derived from human CREST serum)	Antibodies Incorporated	Cat# 15-235-0001; RRID:AB_2797146
Phospho RPA32 (S4/S8) rabbit polyclonal Antibody (company quality control positive signal after etoposide, negative after alkaline phosphatase treatment. Does not stain RPA32 mutant with serines turned to alanine (Zuazua-Villar et al., 2015; Liu et al., 2012). Figure S4C shows ATR dependent phosphorylation.	Bethyl laboratories	Cat# A300-245A; OWL ID: 54194
Phospho-Histone H2A.X (Ser139) (20E3) Rabbit mAb. UV induces signal, which is inhibited with blocking peptide or phosphatase treatment.	Cell Signaling Technology	Cat# 9718; RRID:AB_2118009
Anti IdU antibody	BD Biosciences	Cat# BD 347580; RRID:AB_400326
Anti ssDNA antibody	Millipore	Cat# MAB3034
Anti-Oct-3/4 antibody (C10)	Santa Cruz Biotechnology	Cat# sc-5279; RRID:AB_628051
Alexa Fluor 488 Donkey Anti-Rabbit IgG (H+L) Antibody	Thermo Fisher Scientific	Cat# A-21206; RRID:AB_2535792
Alexa Fluor 488 Donkey Anti-Mouse IgG (H+L) Antibody	Thermo Fisher Scientific	Cat# A-21202; RRID:AB_141607
Alexa Fluor 488 Goat Anti-mouse IgG1	Thermo Fisher Scientific	Cat# A21121; RRID:AB_2535764
Alexa Fluor 555 Donkey Anti-Rabbit IgG (H+L)	Thermo Fisher Scientific	Cat# A-31572; RRID:AB_162543
Alexa Fluor 555 Donkey Anti-Mouse IgG (H+L)	Thermo Fisher Scientific	Cat# A-31570; RRID:AB_2536180
Goat anti-Rat IgG (H+L) Secondary Antibody, Alexa Fluor 555	Thermo Fisher Scientific	Cat# A-21434; RRID:AB_2535855
CF 568 Goat Anti-Mouse IgG2a	Biotium	Cat# 20258

(Continued on next page)

Continued

REAGENT or RESOURCE	SOURCE	IDENTIFIER
Alexa Fluor 647 Donkey Anti-Rabbit IgG (H+L)	Thermo Fisher Scientific	Cat# A-31573; RRID:AB_2536183
Alexa Fluor 647 Donkey Anti-Mouse IgG (H+L)	Thermo Fisher Scientific	Cat# A-31571; RRID:AB_162542
Alexa Fluor®647 Goat Anti-Rat IgG (H+L)	Thermo Fisher Scientific	Cat# A-21247; RRID:AB_141778
Goat anti-Human IgG (H+L) Cross-Adsorbed Secondary Antibody, Alexa Fluor 488	Thermo Fisher Scientific	Cat# A-11013; RRID:AB_2534080
RPA 32 phospho S33 rabbit polyclonal Company quality control shows positive signal after etoposide. Does not react to S33A mutant (Anantha et al., 2007). Figure S4C shows ATR dependent phosphorylation.	Bethyl Laboratories	Cat# A300-246A
Biological samples		
Human oocytes	Columbia University Fertility Center	N/A
Donated IVF embryos	East Coast Fertility Centers	N/A
Sperm	Columbia University Medical Center	N/A
Chemicals, peptides, and recombinant proteins		
Alt-R S.p. Cas9 Nuclease V3	IDT DNA	Cat# 1081058
CytochalasinB	Sigma Aldrich	Cat# C2743
5-Ethynyl Uridine (EU)	ThermoFisher Scientific	Cat# E10345
5-Iodo-2'-deoxyuridine (IdU)	Sigma Aldrich	Cat# I7125
5-Iodo-2'-deoxyuridine (CldU)	Sigma Aldrich	Cat# C6891
DMSO	Sigma Aldrich	Cat# D2650
PBS	LifeTechnologies	Cat# 14190-250
Triptolide	Sigma Aldrich	Cat# T3652
Alpha Amanitin	Sigma Aldrich	Cat# A2263
Aphidicolin	Sigma Aldrich	Cat# A0781
ATR inhibitor ATR45 (VE-821)	This manuscript: (Charrier et al., 2011)	N/A
AZD7762 (CHK1&CHK2 inhibitor)	Selleckchem	Cat# S1532
LY2603618 selective CHK1 inhibitor (King et al., 2014)	Tocris	Cat# 6454
MK1775 (WEE1 inhibitor)	Selleckchem	Cat# S1525
HEPES	Sigma Aldrich	Cat# H4034
d-sorbitol	Sigma Aldrich	Cat# S3889
Fatty acid free BSA	Millipore Sigma	Cat# 126575
Calcium acetate	Sigma Aldrich	Cat# 21056
Magnesium acetate	Sigma Aldrich	Cat# M2545
Mirin (MRE11 exonuclease inhibitor)	Sigma Aldrich	Cat# M9948
PFM01 (MRE11 endonuclease inhibitor) (Shibata et al., 2014)	Tocris	Cat# 6222
Acetic acid	LabChem	Cat# LC101003s
Methanol	Sigma Aldrich	Cat# 322415
Triton X-100	Sigma Aldrich	Cat# T8787
Ethylenediaminetetraacetic acid (EDTA)	Sigma Aldrich	Cat# E6758
Sodium dodecyl sulfate (SDS)	Sigma Aldrich	Cat# L3771
Tris base	Sigma Aldrich	Cat# T1503
HCl	Fisher Scientific	Cat# A144sl-212
Acidic Tyrode's solution	EMD Millipore	Cat# MR-004-D

(Continued on next page)

Continued

REAGENT or RESOURCE	SOURCE	IDENTIFIER
Olaparib	Selleck Chemicals	Cat# S1060
Hyaluronidase	Sigma Aldrich	Cat# H4272
Puromycin	Thermo Fisher	Cat# A1113802
PMSG, pregnant mare serum gonadotropin	ProSpec	Cat# HOR-272
hCG, human chorionic gonadotropin	EMD Millipore	Cat# 230734
Ionomycin	Sigma Aldrich	Cat# I3909
Paraformaldehyde	Santa Cruz Biotechnology	Cat# sc-281692
Hoechst33342	Life Technologies	Cat# H3570
Proteinase K	Sigma Aldrich	Cat# P4850
Critical commercial assays		
Click-iT EdU Alexa Fluor 555 Imaging Kit	Life Technologies	Cat# C10338
Click-iT EdU Alexa Fluor 488 Imaging Kit	Life Technologies	Cat# C10337
Deposited data		
Single cell sequencing data from human and mouse preimplantation embryos	Sequence Read Archive (SRA)	PRJNA699630, PRJNA693628, PRJNA755329,
Experimental models: Cell lines		
Human oocytes	This paper; Columbia University Fertility Center	N/A
Donated IVF embryos	This paper; East Coast Fertility Centers	N/A
Sperm	This paper; Columbia University Medical Center	N/A
Experimental models: Organisms/strains		
Homo sapiens	This paper	N/A
Mouse: B6D2F1	The Jackson Laboratory	Cat# 100006
Oligonucleotides		
gRNA for Cas9 RNP assembly. Table S2 ; 5'-AATGAAGGGCTGCTGTATCG	This paper; Integrated DNA Technologies	N/A
Software and algorithms		
bwa-0.7.17	This manuscript: (Li and Durbin, 2009)	https://github.com/lh3/bwa/releases/tag/v0.7.17
samtools-1.11	This manuscript: (Danecek et al., 2021)	http://www.htslib.org/download/
QDNAseq v1.26.0	This manuscript: (Scheinin et al., 2014)	https://cran.r-project.org/bin/macosx/scientific-software/prism/
Prism	GraphPad	https://www.graphpad.com/scientific-software/prism/
Zen confocal imaging and image processing software	Zeiss	https://www.zeiss.com/microscopy/us/products/microscope-software/zen.html
Other		
Male-FactorPak collection kit	Apex Medical Technologies	Cat# MFP-130
Piezo micropipette	Origio	Cat# Piezo-20-15
10%PVP	Irvine Scientific	Cat# 90123
Mineral oil	Sigma Aldrich	Cat# 330779-1L
Holding pipette	Origio	Cat# MPH-MED-30
ICSI micropipette	Origio	Cat# MIC-SI-30
Glass bottom dishes for imaging	MatTek	Cat# P35G-1.5-10-F
Glass bottom dishes for manipulations	MatTek	Cat# P60G-1.5-30-F
Single cell lysis and fragmentation buffer	Sigma Aldrich	Cat# L1043
NEBNext Ultra II DNA Library Prep Kit for Illumina	New England Biolabs	Cat# 6040S

(Continued on next page)

Continued

REAGENT or RESOURCE	SOURCE	IDENTIFIER
NEBNext Multiplex Oligos for Illumina	New England Biolabs	Cat# E6609S
SEQPLEX Enhanced DNA Amplification Kit	Sigma Aldrich	Cat# SEQXE
ProLong Gold Antifade Mountant	Thermo Fisher Scientific	Cat# P36930
ECMPC warming solution set	ECMPC	Cat# ECMPC-220
Quinn's Advantage Thaw Kit	Cooper Surgical	Cat# ART-8016
Vitrification kit	Cryotec	Cat# 101
Warming kit	Cryotec	Cat# 102
Global Total	LifeGlobal	Cat# H5GT-030
Quinn's Sperm washing medium	CooperSurgical	Cat# ART-1005
Sperm freezing medium	Irvine Scientific	Cat# 90128
Sperm separation kit Isolate	Irvine Scientific	Cat# 99264
Global Total w. HEPES	LifeGlobal	Cat# LGTH-050
G-MOPS Plus	Vitrolife	Cat# 10130

RESOURCE AVAILABILITY

Lead contact

Further information and requests for resources should be directed to and will be fulfilled by the Lead Contact, Dieter Egli (de2220@cumc.columbia.edu).

Materials availability

This study did not generate unique reagents.

Data and code availability

Data are available at SRA BioProject accession numbers SRA: PRJNA699630, SRA: PRJNA693628, and SRA: PRJNA755329. No code specific to this study was generated.

EXPERIMENTAL MODEL AND SUBJECT DETAILS

Human subjects

The Columbia University Institutional Review Board, the Columbia University Embryonic Stem Cell Committee approved all human procedures to obtain human oocytes for this research, including for low pass genome sequencing and public database submission. Gamete and embryo donors provided informed consent, and followed guidance provided by New York State Stem Cell Science (NYSTEM, <https://stemcell.ny.gov/new-model-informed-consent-forms>). The experience of oocyte donors in research is described in a prior study (Zakarin Safier et al., 2018).

Human oocytes

Human oocytes designated for research were obtained from donors following routine gonadotropin releasing hormone antagonist *in vitro* fertilization stimulation at the Columbia University Fertility Center. Ovarian stimulation was monitored with regular ultrasound and serum hormonal assays per practice protocol (Palmerola et al., 2018). Oocyte retrieval was performed by transvaginal ultrasound-guided needle aspiration under intravenous sedation. Oocytes were vitrified using Cryotech vitrification kit and stored in liquid nitrogen until use. For experimental procedures, oocytes were thawed using the Cryotech Warming Kit (Cryotech, Tokyo, Japan) or the ECMP warming solution set, then exposed to experimental conditions as outlined below. For the ensuing human oocyte studies, "control media" refers to Global Total. All experiments were conducted during incubation at 37°C with 5% CO₂ and 20% O₂. Donated oocytes were used for experiments involving artificial activation and for experiments involving timing of DNA replication in zygotes, Cas9 injection, as well as for ICSI followed by aphidicolin incubation. Human oocytes were randomly allocated to experimental groups.

Human embryos

Cryopreserved human cleavage-stage and blastocyst embryos and unfertilized oocytes were anonymously donated from individuals and couples who provided consent for use in research. Embryos were of good quality and had been cryopreserved for potential clinical use, but were then no longer needed and donated for research. The cause of treatment is not disclosed. Range of maternal age of

donated embryos is between 27–43. Embryos of both sexes were used, as provided by the unbiased fertilization of oocytes with sperm carrying either a Y or X chromosome. Cleavage stage embryos were thawed using the one-step thaw protocol using Global total with HEPES. Blastocyst stage embryos were thawed using the Quinn's Advantage thaw kit, then exposed to experimental conditions as outlined below. Vitrified embryos were thawed with the ECMPC warming solution set. Embryo culture was performed in Global Total. All experiments were conducted during incubation at 37°C with 5% CO₂ and 20% O₂.

Sperm donation and processing

Human sperm was obtained following donation from living donors following masturbation after 2–5 days of abstinence and collected in a Male-FactorPac collection kit. Sperm was cryopreserved using commercially prepared density gradient (Isolate) and centrifugation was used to isolate motile sperm. The resultant sperm pellet was resuspended in sperm prep medium (Quinn's Sperm Washing Medium, Origio), centrifuged and washed repeatedly prior to cryopreservation using freezing medium (Irvine Scientific, 90128). Cryopreservation was performed using a time-based freezing protocol with gradually lowered temperature time sets then stored in liquid nitrogen at less than -196°C until use. Samples were thawed at 38–40 °C for a maximum of 10 min and transferred to a 15mL conical tube. Quinn's Sperm Washing Medium was added dropwise to achieve a volume of 6mL. Samples were centrifuged at 300x g for 15min. Supernatant was removed and an additional wash with centrifugation was performed. The supernatant was removed following a second wash, sperm pellets resuspended in wash media, then analyzed for viability. Sperm was mixed on the stage of a microscope with 10%PVP, and individual motile sperm were immobilized by pressing the sperm tail with the ICSI micropipette to the bottom of the dish, then picked up for injection. Donated sperm was used to determine the timing of DNA replication in zygotes, as well as for ICSI followed by aphidicolin incubation.

Murine oocytes

The Columbia Institutional Animal Care and Use Committee approved animal protocols. Mouse oocytes were obtained as described previously (Yamada and Egli, 2017). Briefly, B6D2F1 female mice (Jackson strain #100006) were superovulated at 5–7 weeks of age by injection with 5 IU of pregnant mare serum gonadotropin (ProSpec) followed 48–52h later by 5 IU of human chorionic gonadotropin (EMD Millipore). Mice were sacrificed 14–15 hours later and oviducts were removed. Oocyte-cumulus complexes were isolated from the oviduct in a dish containing droplets of GMOPsplus (Vitrolife) containing 300 µg/mL hyaluronidase (Sigma-Aldrich), covered with mineral oil on the heated stage of an Olympus SZ51 microscope. Oocytes were and then washed and cultured in Global Total until experimental use.

METHOD DETAILS

Embryo culture and Drug incubations

Embryos, mouse and human, were cultured in Global Total (Life-Global) for the duration of the experiments and with added compounds as outlined below.

Incubation in RNA polymerase inhibitors triptolide (1 µM) or alpha amanitin (20 µg/ml) was performed from the 2PN stage (day1) to day3 of human development. Incubation in aphidicolin was performed at 2 µM. This concentration of aphidicolin has been shown to prevent the formation of ssDNA gaps through uncoupling of leading and lagging strand synthesis (Ercilla et al., 2020). CHK1/CHK2 inhibitor AZD7762 (Zabludoff et al., 2008) at 100nM, CHK1 inhibitor LY2603618 (King et al., 2014) at 2.5 µM, Wee1 kinase inhibitor MK1775 (Hirai et al., 2009) at 500nM and ATR inhibitor ATR45 (VE-821), which shows selectivity of >600x over related kinases ATM or DNA-PK (Charrier et al., 2011), at 1 µM, except for zygotes at the 1-cell stage which were incubated for 4 hours at 2.5 µM ATR45. PFM01 (Shibata et al., 2011) was used at 50 µM, and human zygotes were incubated from 14–19h post activation, while mouse zygotes were incubated from 11.5–15.5h post activation in aphidicolin and either mirin or PFM01. Mirin was used at a concentration of 50 µM. Olaparib was used to inhibit PARP at a concentration of 10 µM. All experiments were conducted during incubation at 37°C with 5% CO₂ and 19–20% O₂. Chemical stock solutions were prepared in DMSO at concentrations at least 1000x higher than the final concentration.

Cas9 RNP preparation and injection

gRNA was obtained from Integrated DNA Technologies (IDT). For ribonucleoprotein (RNP) preparation, 2 µL of 63 µM IDT nlsCas9 v3, 3 µL of injection buffer, and 1.5 µL of 100 µM sgRNA were mixed and kept at room temperature for 5 minutes. Thereafter, 96.5 µL of injection buffer consisting of 5mM Tris-HCl, 0.1mM EDTA, pH 7.8 was added prior to injection. gRNA targets on chr6, chr11, chr16 and chr17 are provided in the legend of Table S2. Injection was performed into metaphase MII oocytes.

Artificial activation

Artificial activation of human MII oocytes was performed using two pulses of 2.7kV/cm at 50 µs using ECFG21 (Nepagene) in fusion buffer consisting of 0.25 M d-sorbitol buffer containing 0.1 mM calcium acetate, 0.5 mM magnesium acetate, 0.5 mM HEPES, and 1 mg ml⁻¹ fatty-acid-free BSA as previously described (Tachibana et al., 2013). Thereafter, oocytes were incubated for 3.5–4h in 10 µg/ml puromycin, followed by a wash step and following culture in Global total.

Mouse oocytes were activated at 1-6 hours post retrieval using 2 μ M ionomycin (Sigma Aldrich) in Global Total medium for 5 minutes at 37°C followed by culture in 10 μ M puromycin and 5 μ g/ml cytochalasin B for 3 hours, then cytochalasin B only for 2 hours and 10 minutes to prevent second polar body extrusion.

Immunocytochemistry of Human and Murine Embryos

Following the experimental exposures, mouse and human embryos were fixed in 2% paraformaldehyde (PFA) and 0.25% Triton X-100 in PBS for 10 minutes at room temperature, serially washed in phosphate-buffered solution (PBS) at room temperature, then stored in PBS at 4°C until staining and imaging. Embryos were placed in 10-20 μ l droplets of primary antibody solution ([key resources table](#)) within plastic tissue culture dishes covered with mineral oil for 1 hour at room temperature, serially washed (x2) in PBS containing 0.01% Triton X-100 to prevent embryos sticking to oil, then transferred to 10-20 μ l secondary antibody solution and Hoechst (dilution 1:500) for 30 minutes. Embryos were then serially washed (x2) and placed in 5 μ l droplets of PBS with 0.5% serum albumin in uncoated glass bottom dishes (Mattek) covered with embryo culture oil for imaging. The following primary antibodies were used across experiments as described above: Oct-4, γ H2AX, RPA32, RPA32 S4/S8, RPA32 S33, 53BP1, RAD51, Centromere, phospho-CHK1 ([key resources table](#)). Phospho-specific antibodies were quality controlled through ATR dependence of foci formation in mouse zygotes, and for γ H2AX also in human zygotes ([Figures 1E and S4](#)). The RPA32 phospho S33 antibody does not react to an S33A mutant ([Anantha et al., 2007](#)). The Anti-phospho-Histone H2A.X-Ser139 mouse monoclonal antibody does not react to S139A in human pluripotent stem cells ([Orlando et al., 2021](#)). The RPA32 (S4/S8) rabbit antibody does not stain RPA32 mutant with serines turned to alanine ([Zuazua-Villar et al., 2015](#); [Liu et al., 2012](#)). The appropriate secondary antibodies conjugated with Alexa Fluor 488, Alexa Fluor 555, CF 568, or Alexa Fluor 647 were diluted at 1:500-1:1000 ([key resources table](#)).

Ethynyl deoxyuridine (EdU) labeling of zygotes and embryos was performed using the labeling kit (Thermo Fisher Scientific) as described by the manufacturer. 10 μ M EdU was added to culture medium for 1 h at the indicated time points, and cells were harvested and fixed thereafter. 5-ethynyl uridine (EU) labeling was performed by incubating day3 cleavage stage embryos for 4 hours in Global total containing 0.2mM EU.

DNA fiber analysis

DNA fiber analysis was performed in mouse 1-cell embryos at 5.5h post activation, in late G2 phase from 12-15h post activation, in 8-cell embryos at 52h post activation, and in blastocysts at 96h post activation. Human 1-cell embryos were labeled 6h post activation, and donated day3 and day6 embryos were labeled within 3-4h after thawing. Incubation was performed in 25 μ M IdU or 25 μ M CldU for 30min. Digestion of zona pellucida by Acidic Tyrode's solution was performed in a 4-well dish at room temperature at ambient atmosphere for 1-5 minutes using continuous observation under a stereomicroscope, and then neutralized in culture medium. \sim 30 cells were collected in 0.5-1 μ l medium and placed in a PCR tube, lysed by adding 30 μ l of fresh pre-warmed (30 °C) spreading buffer (0.5% SDS, 200mM Tris pH 7.4, 50 mM EDTA), incubated for 6 min at RT and stretched using gentle tilting on regular microscope slide. Slides were fixed for 2 min at RT in cold 3:1 methanol: acetic acid, air dried at RT, and then incubated in 2.5M HCl for 30 min, rinsed 5 times with PBS, and blocked with 3% BSA in PBS for 1h. DNA fibers were stained for 1h with anti-ssDNA and anti-BrdU/IdU antibodies. Afterwards, slides were rinsed 4 times in PBS, incubated 1h with secondary antibodies (Goat anti-mouse IgG1, #A21121; Goat anti-mouse IgG2a, #20258), mounted with ProLong Gold Antifade mountant and let dry overnight. The fiber tracks were imaged on a Nikon Eclipse 90i microscope fitted with a PL Apo 40X/0.95 numerical aperture objective and measured using ImageJ software v1.53.

The length of each track was determined manually using the segmented line tool on ImageJ software. The pixel values were converted into μ m using the scale bar generated by the microscope software. The extension of the DNA fibers was calculated as follows: 2.59 ± 0.24 kbp/ μ m according to ([Jackson and Pombo, 1998](#)). In [Figure 2](#), sister fork ratio was calculated as shorter fork/longer fork, with bidirectional forks only. Forks were considered asymmetric with a ratio <0.75 as ([Bester et al., 2011](#)).

Confocal microscopy and DNA damage foci analysis

Embryos were imaged with confocal microscopy using a Zeiss LSM (LSM 710) at a magnification of 63X and the Zeiss Zen software. Images were obtained using 488-, 543- and 633-nm lasers and bright-field microscopy. The number of confocal sections was adjusted to capture the entire nucleus or the entire embryo according to the experimental design as described above. Cell numbers and staining foci numbers were counted manually. Nuclei were identified by the presence of Hoechst33342. Foci were identified if at least 3x greater intensity than nuclear average, spherical in appearance, and overlapping with Hoechst33342 staining. Inner cell masses were identified by the presence of Oct4 within a blastocyst embryo. Active DNA replication was identified by the presence of EdU. DNA damage was identified by the detection of γ H2AX and RPA foci within the nucleus. Mechanisms of DNA repair were identified through the detection of RPA S4/S8, RPA S33, Rad51 and 53BP1 foci within the nucleus.

Single-cell/single nuclei whole genome amplification and sequencing

Single cells from blastomeres were collected on the heated stage (Tokai Hit) of an Olympus IX71 inverted microscope equipped with Narishige micromanipulators and a zona pellucida laser (Hamilton-Thorne). Single nuclei were isolated from blastomeres by lysis and dissection of different nuclei using two 20 μ m diameter Piezo micropipettes and Holding pipette (Origio). Single embryo cells or nuclei were placed manually in single wells of a 96-well plate containing 9 μ l of lysis buffer, prepared as a master mix of 798 μ l H₂O, 6 μ l of 10 mg/mL Proteinase K solution (Sigma-Aldrich), and 96 μ l 10X Single Cell Lysis and Fragmentation buffer (Sigma-Aldrich). Single

cells / single nuclei were lysed by heating 96-well plates containing single cells / single nuclei at 50°C for 1 hour, followed by incubation at 99°C for four minutes using a PCR thermocycler. Single-cell / single-nuclei whole genome amplification (WGA) using degenerate oligo-nucleotide priming PCR (DOP-PCR) was performed using the SEQPLEX Enhanced DNA Amplification Kit (SEQXE, Sigma) according to the manufacturer's instructions. In addition, a modified version of the DOP-PCR protocol that allows inline indexing of WGA DNA was also applied. WGA DNA was subsequently processed for Illumina library sequencing preparation using standard TruSeq indexing methods via the NEBNext Ultra II DNA Library Prep Kit for Illumina (New England Biolabs). NEBNext Multiplex Oligos for Illumina (96 index primers) were used for four amplification cycles. Library DNA was quantified using Qubit dsDNA HS Assay Kit (Invitrogen, Carlsbad, CA, USA) and library size distribution was confirmed using a 2100 Bioanalyzer DNA 1000 Kit (Agilent, Santa Clara, CA, USA). A unimodal curve centered around 300 – 500 bp was scored as a successful library preparation. Subsequently, 30 μ L of each pooled library was sent for sequencing at a concentration of 20ng/ μ L. Multiplex sequencing was performed using Illumina HiSeq 2500 single end indexed run (SR100) while targeting a coverage of \sim 1 million reads per cell/nuclei, sufficient for quantitative genome-wide copy number analysis.

Single-cell / single-nuclei sequencing analysis and copy number inference

Analysis of DNA sequencing data was performed as previously described (Baslan et al., 2015) with minor modifications as outlined below. Briefly, multiplex sequencing data were demultiplexed according to unique barcodes with reads assigned to their respective single-cell or single-nuclei. Unique reads were aligned to the reference human and mouse genome builds, hg19 and mm9, respectively. Each genome was partitioned into 5000 bins using a previously described algorithm (Varbin) that corrects for genome sequence mappability (Baslan et al., 2012; Navin et al., 2011). Uniquely mapped reads were sorted, indexed and subsequently counted within the partitioned genomic bins. For single-cell copy number inference, read count data were normalized genome-wide followed by CBS segmentation (Olshen et al., 2004) and transformed into integer copy number states using a least-squares fit approach (Baslan et al., 2015).

Copy number inference from single-nuclei sequencing data was performed similarly with the exception that bin read counts were initially processed using Kernel Density Estimation (KDE) resulting in two primary densities. One density contained very low read counts and was attributed to index switching during Illumina multiplex library sequencing, a known sequencing artifact (Larsson et al., 2018). Bins constituting this density were normalized and transformed to a ground state (i.e. nullisomy). The second density contained high read counts in different genomic positions in one or more chromosomes across different single-nuclei. Read counts were processed similarly to single-cell data with the exception that segments were designated as “copy number states” (compared to absolute integer) given the inherent uncertainty of the absolute copy number of the segments in spontaneous micronuclei.

For increased resolution of break point mapping, additional analysis with bin size of 10kb, 50kb and 100kb using bwa aligner (v.0.7.17) (Li and Durbin, 2009), samtools (v.1.11) (Danecek et al., 2021), and R package QDNAseq v1.26.0 (Scheinin et al., 2014) was performed and results evaluated for consistency with analysis using 500kb bins described above (Baslan et al., 2015). All break point calls were also manually inspected on copy number plots and read number files independently by two researchers. Parthenogenetic 1-cell embryos were haploid, enhancing signal differences, and allowing for increased resolution of chromosomal break mapping to 10-50kb.

Break site annotations

Annotation of break sites was performed as follows: transition points in segmented raw read count data were flagged across single-cell / single-nuclei datasets with subsequently manual curation using the University of California Santa Clara (UCSC) Genome Browser and transition point coordinates. A site was considered fragile if it occurred independently within the same or a neighboring bin (according to Baslan et al., 2015) in at least three different embryos. A fragile area is defined by the bin coordinates within which the breaks fall (as in Figure 4 for CNTN5). Gene density comparison in Figure 5G was performed by selecting random locations within hg19 genome assembly using bedtools v2.30.0 (Quinlan and Hall, 2010). Complete transcripts and adjacent intergenic areas were included in 1-2Mb intervals to calculate the density of protein-coding genes. The genome average density of protein coding genes of \sim 6.9 genes/Mb is based on an estimated 21,306 protein-coding genes (Pertea et al., 2018) and a human genome size of 3.1 billion base pairs.

QUANTIFICATION AND STATISTICAL ANALYSIS

Analysis of DNA damage and embryo development

Statistical analyses were performed on GraphPad Prism (GraphPad Software, Inc., La Jolla, CA, USA). Embryo groups were compared using one-way analysis of variance (ANOVA) with Bonferroni correction for multiple comparisons where appropriate, and using Student's t-test for comparison between two groups. Fisher's exact test was performed using <https://www.socscistatistics.com/> to analyze sister fork asymmetry at different developmental stages, and to analyze development of human embryos with and without CHK1 inhibitor as indicated in Figure Legends. Mean and standard deviations are displayed as indicated in Figure Legends. The number of *n* indicated in the Figures represents the number of cells. In the case of zygotes, the number of embryos and the number of cells is equivalent.

Supplemental figures

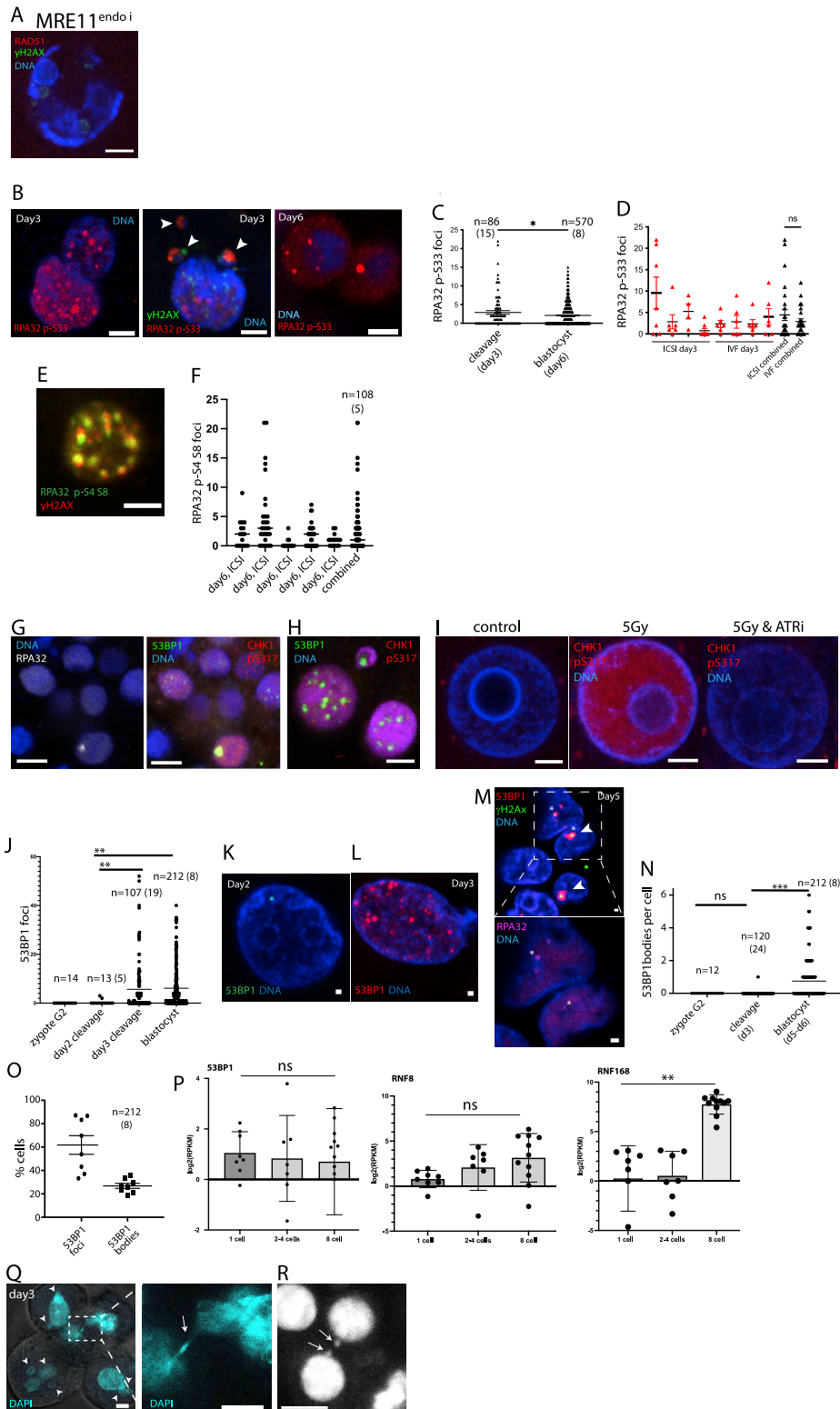


Figure S1. Markers of DNA replication stress in human preimplantation embryos, related to Figure 1

- (A) Human parthenote treated with MRE11 endonuclease inhibitor PFM01 according to Figure 1D, at 18 h post activation and with immunostaining for γ H2AX and RAD51. Scale bars, 5 μ m.
- (B) Quantification of foci for RPA32 phosphorylated at serine 33 at the cleavage and the blastocyst stage. Statistics using Student's t test. * $p < 0.05$.
- (C) Immunostaining for RPA32 phosphorylated at serine 33 of blastomere at indicated stages. Arrowheads indicate micronuclei. Scale bars, 5 μ m.
- (D) Quantification of foci for RPA32 phosphorylated at serine 33 in individual cleavage-stage embryos, with the method of fertilization indicated.
- (E) Immunostaining for RPA32 phosphorylated at serine 4 and serine 8 at the blastocyst stage. Scale bars, 10 μ m.
- (F) Quantification of foci for RPA32 p-S4S8 in individual blastocyst-stage embryos.
- (G) Immunostaining for CHK1 phosphorylated at serine 317. Note the 53BP1 body with unreplicated DNA marked by RPA in the same cell and the elevated signal of phosphorylated CHK1. Scale bars, 10 μ m.
- (H) Immunostaining for CHK1 phosphorylation on Ser 317 and 53BP1.
- (I) Antibody quality control at the 1-cell stage. ATR-dependent phosphorylation of CHK1 at Ser 317 in mouse embryos irradiated with 5Gy 1 h after irradiation. 20/20 nuclei showed p-S317 staining, whereas 0/20 in the ATR-inhibited and 0/20 in unirradiated control samples showed staining ($p = 0.00001$, Fisher's exact test). Scale bars, 5 μ m.
- (J) Developmental progression of 53BP1 focus formation distinguishing day-2 and -3 cleavage-stage embryos. Statistical analysis using one-way ANOVA. ** $p < 0.001$.
- (K and L) Immunostaining for 53BP1 on day 2 (K) and day 3 (L) of development. Note the increase in foci number. (Secondary antibodies coupled to AF488 or AF555 were used.) Scale bars, 1 μ m.
- (M) 53BP1 bodies in a day 5 blastocyst. Arrowheads indicate the symmetry of 53BP1 bodies in neighboring cells. RPA32 positive foci demonstrating single-stranded unreplicated DNA are indicated with an asterisk and shown in the lower panel.
- (N) Frequency of 53BP1 bodies depending on the developmental stage. Statistical analysis using Student's t test. The 53BP1 bodies follow the formation of foci with a delay of one or more cell cycles.
- (O) Percentage of cells in day 5 blastocysts with 53BP1 bodies ($>1\text{-}\mu\text{m}$ diameter) or 53BP1 foci ($<1\text{-}\mu\text{m}$ diameter). The horizontal bar indicates average.
- (P) Analysis of RNA-seq data from GSE44183 (Xue et al., 2013), for 53BP1, RNF8, and RNF168 from the one-cell stage to embryonic genome activation in human embryos. Individual data points are individual single cells. ** $p < 0.001$ using one-way ANOVA.
- (Q) Micronucleation (arrowheads) and chromatin bridge (enlarged panel) in a day-3 cleavage-stage embryo. Scale bars, 10 μ m.
- (R) Chromatids with the delayed resolution of cohesion in sister cells of a day 5 blastocyst, suggesting unresolved replication intermediates. These defects are characteristic of chromosome segregation defects seen after somatic cell nuclear transfer, which are induced by abnormal DNA replication, rather than by abnormal spindle function (Chia et al., 2017). Scale bars, 5 μ m.

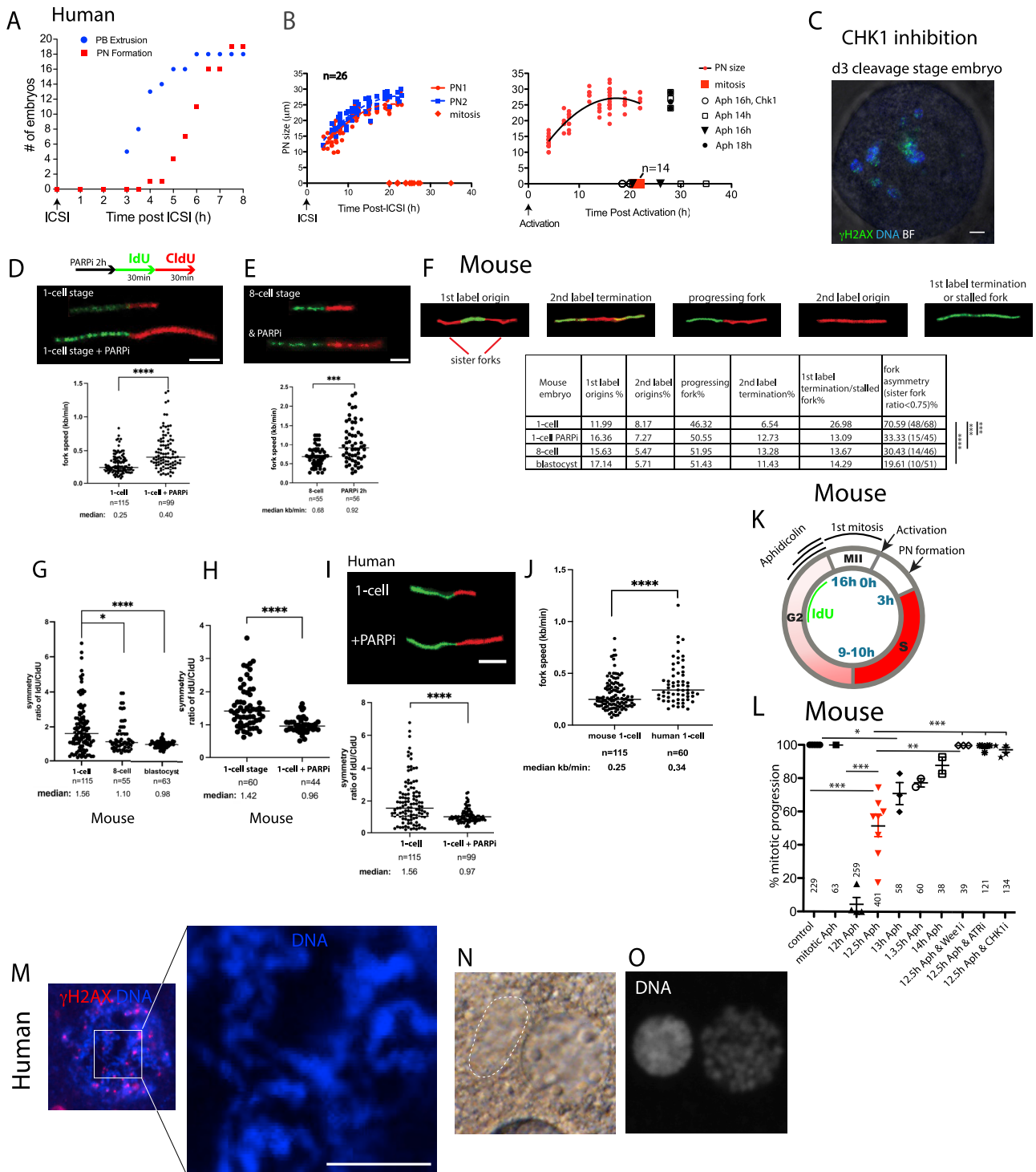


Figure S2. Cell-cycle progression of fertilized eggs and parthenotes, related to Figure 2

(A) Timing of polar body extrusion and pronucleus formation after intracytoplasmic sperm injection (ICSI) of human oocytes.

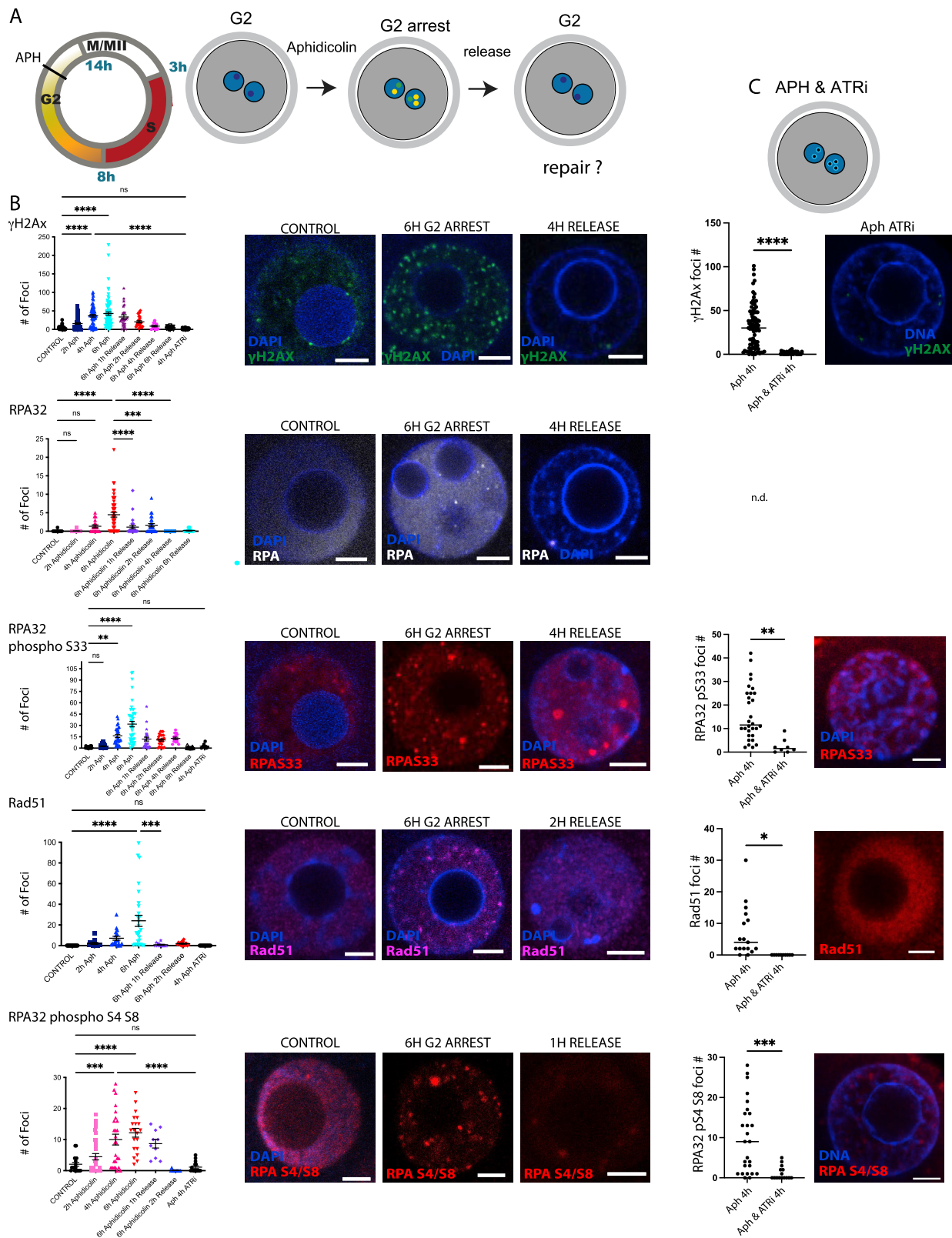
(B) Pronucleus size during the first cell cycle and timing of mitotic entry after fertilization or parthenogenesis in human oocytes. Symbols on the x axis indicate the time point of entry into mitosis.

(C) Human cleavage-stage embryo incubated from day 3 to 6 in CHK1 inhibitor AZD7762. Note the highly fragmented nucleus and genome. Scale bars, 5 µm.

(D and E) DNA replication fork speed in mouse embryos with and without PARP inhibition using Olaparib and sister fork asymmetry in mouse 1-cell (D) and 8-cell (E) embryos.

(legend continued on next page)

-
- (F) Representative DNA replication structures and the quantification of replication forks. $n > 300$ replication fork and $n > 45$ bidirectional forks per developmental stage. The table includes the same sister fork ratio data as in [Figure 2P](#).
- (G–I) Replication track ratio first/second label through preimplantation development (G) and with PARP inhibition using Olaparib in mice (H) and humans (I).
- (J) Comparison of replication fork speed at the mouse and human 1-cell stage is also shown. Fork speed was calculated as follows: 2.59 ± 0.24 kbp/ μm according to [Jackson and Pombo \(1998\)](#).
- (K) Schematic of the experiment in mice. Aphidicolin is added with or without additional compounds in late G2 phase of the cell cycle. Entry into the first mitosis is monitored.
- (L) Percentage of mouse embryos progressing from G2 to the first mitosis depending on the timing of aphidicolin application. The total numbers of eggs are indicated for each condition. Each dot represents an independent experiment consisting of at least ten embryos. Wee1i = Wee1 inhibitor. Statistical analysis using Student's t test.
- (M) Human parthenogenetic 1-cell embryo (zygote) incubated from 15.5 h post activation in aphidicolin for 6 h. Note the individual chromatids demonstrating chromosome condensation, though condensation is not as condensed as complete as in metaphase chromosomes. Scale bars, 5 μm , related to [Figure 5D](#).
- (N) 2PN zygote with asymmetric nuclear envelope breakdown after aphidicolin exposure. The asymmetry persisted for more than 5 h.
- (O) 2PN zygote with asymmetric chromosome condensation in the two pronuclei. Scale bars, 5 μm .



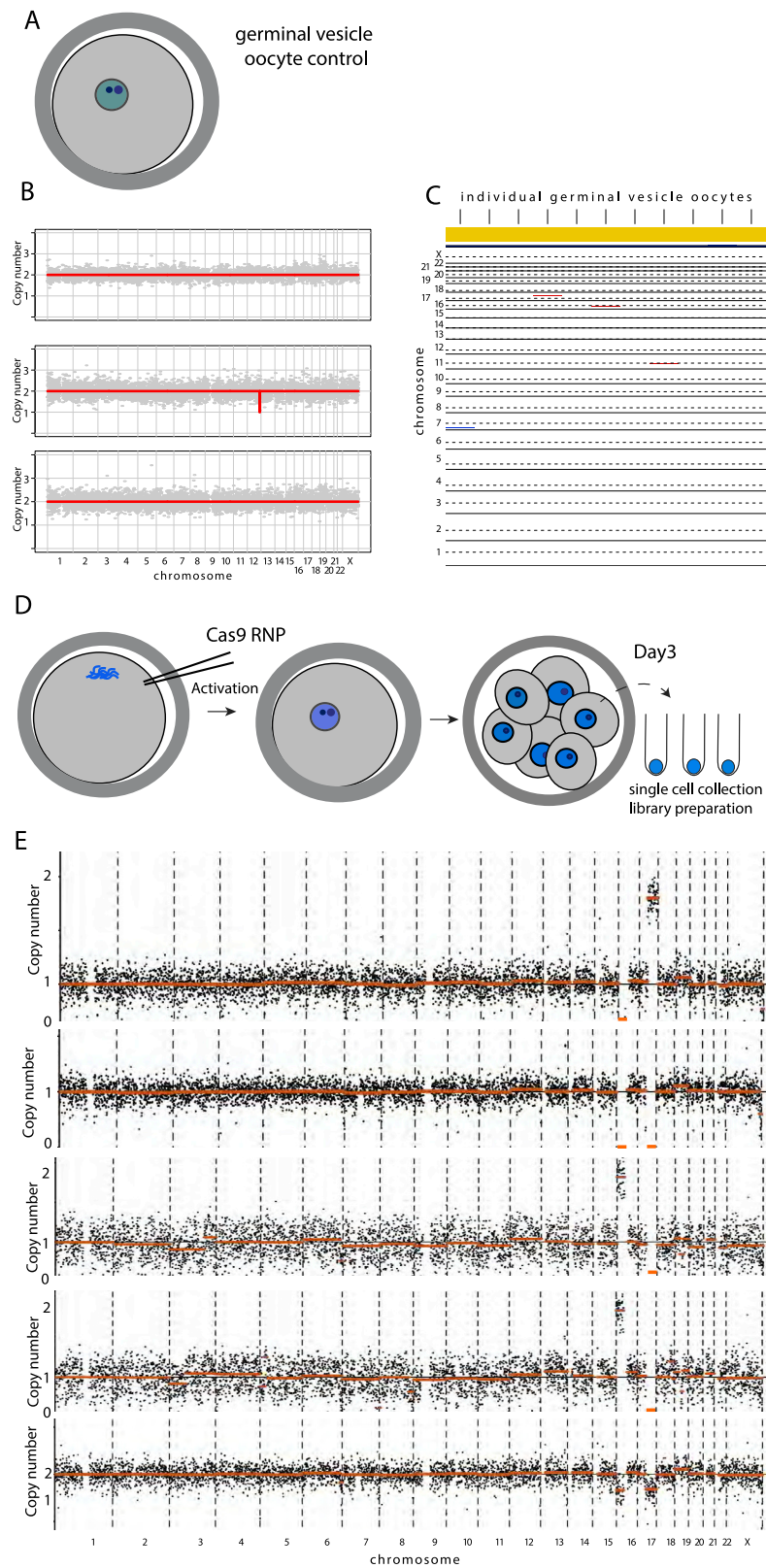
(legend on next page)

Figure S3. DNA damage response to stalled replication forks in G2 of the first cell cycle, related to Figure 2

(A) Experimental schematic. Mouse parthenogenetic embryos were exposed to aphidicolin in G2 at 12 h post activation, and arrested zygotes were analyzed. Stable arrest is defined as 6 h of arrest and 18 h post activation, a time point when all control zygotes are at the 2-cell stage.

(B) Immunostaining for the indicated markers during replication fork stalling and after release. The number of foci per haploid nucleus is shown. *** Indicates $p < 0.0001$. ** Indicates $p < 0.001$. Statistical analysis using one-way ANOVA. Scale bars, 5 μm .

(C) Antibody controls to determine ATR dependence of phospho-RPA, γH2AX foci, and Rad51 foci formation.



(legend on next page)

Figure S4. Controls for chromosome content analysis, related to Figure 3

(A) Cell type being analyzed.

(B) Representative chromosomal content plots of GV oocytes.

(C) Heatmap of chromosomal content. The blue represents a loss and the red a gain. The dashed line represents the position of the centromere.

(D) Schematic of the experiment. The injection of Cas9 RNP into unfertilized oocytes. Artificial activation is used instead of fertilization to initiate the cell cycle and form a haploid parthenote. Blastomeres are collected on day 3.

(E) Chromosomal analysis of a parthenogenetic embryo. Note the segmental changes on chromosomes 16 and 17 including complete loss (nullisomy). The cell at the bottom has diploidized and shows segmental changes in one of two chromosomes. 5 of 6 cells of this embryo were successfully harvested and analyzed.

Figure S5. Chromosome breakage at stalled replication forks causes sister chromatid nondisjunction and segmental nullisomy in haploid human zygotes, related to Figure 6

Analysis of chromosomal break sites after exposure of haploid human zygotes to aphidicolin 16 h post activation, as in schematic of Figure 6A.

(A) Chromosome content plot of an isolated nucleus.

(B) Chromosome 8 content plot of different nuclei from the same cell, each with normalized sequencing read frequency in 100-kb bins indicated in different colors along the chromosome. Vertical bars indicate sites of copy-number transitions. Note the complementarity in different nuclei.

(C) Chromosome content analysis at chr11 at q11-q12.1 (red box) of two nuclei (blue and orange) isolated from the same cell, with normalized sequencing read frequency displayed along the chromosome. Vertical lines indicate copy-number transitions to nullisomy.

(D) Chromosome 1 content plot at p21.2-p13.3 (red box) of two nuclei (blue and orange) isolated from the same cell, with normalized sequencing read frequency displayed along the chromosome. Vertical bars indicate sites of copy-number transition to nullisomy, related to Figure 6.

(E) Chromosome 14 content plot with stepwise transition from 2 to 1 to 0 copies with complementarity. The distance between break points is indicated.

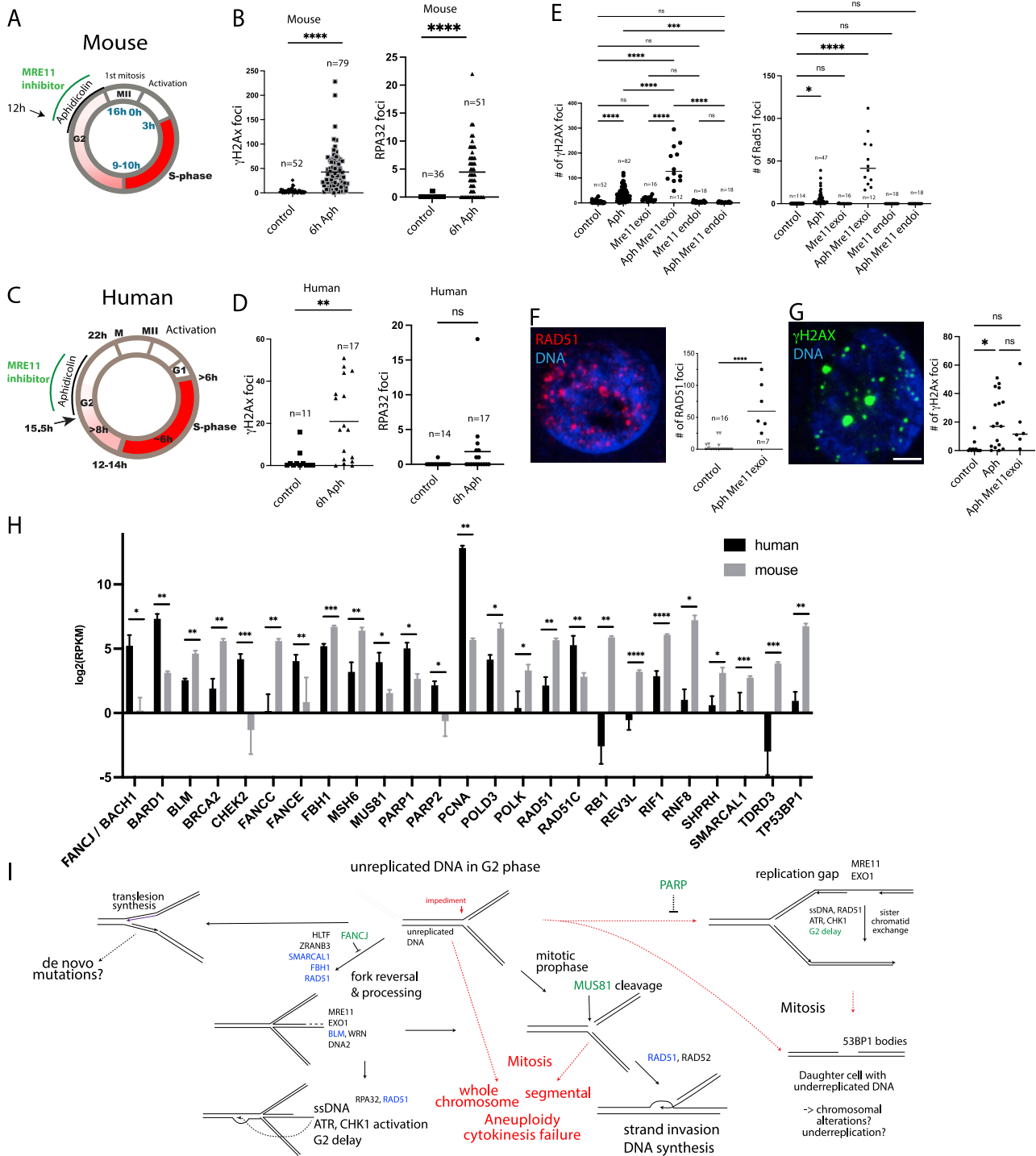


Figure S6. Processing of unreplacated sites is dependent on MRE11, related to Figures 6 and 7

(A–D) Schematic of the timing of application of aphidicolin and/or MRE11 inhibitor in the first G2 phase and the corresponding quantification of γ H2AX and RPA32 foci after 6 h of aphidicolin (Aph) incubation per haploid nucleus in mice (A and B) and human (C and D). The species is indicated below each panel. Horizontal bars indicate averages. Statistical analysis using Student's t test. * $p < 0.05$, ** $p < 0.01$, *** $p < 0.001$, **** $p < 0.0001$.

(E) MRE11 endonuclease or exonuclease dependence of γ H2AX and Rad51 foci formation at forks stalled by aphidicolin. Exonuclease inhibition dramatically increases the number of foci, whereas endonuclease inhibition completely abrogates it. Statistical analysis using one-way ANOVA.

(F and G) Corresponding MRE11 inhibitor study in human parthenotes and quantification of RAD51 (F) and γ H2AX (G) foci.

(legend continued on next page)

(H) Transcript abundance in human and mouse 1-cell stage embryos. The 69 transcripts involved in DSB repair and replication fork stability represented in two datasets containing both mouse and human data GSE44183 (Xue et al., 2013) and GSE18290 (Xie et al., 2010) were analyzed, and the 25 genes shown were differentially expressed in both datasets. Shown are data from Xue et al. Statistical analysis using Welch's t test, * $p < 0.05$, ** $p < 0.01$, *** $p < 0.001$, **** $p < 0.0001$, related to Table S7.

(I) Model for different outcomes of stalled replication forks and postreplicative ssDNA gaps in human and mouse embryos. Genes labeled in green are showing higher transcript levels in 1-cell human embryos than in the mouse, whereas genes labeled in red show lower transcript levels. PARP inhibition by Olaparib is thought to result in increased replication fork progression but also more gap formation. For more details on factors involved in the repair of stalled forks, see the review by Joseph et al. (2020). Red arrows indicate paths to aneuploidy. Whether and how postreplicative ssDNA gaps contribute to aneuploidy are not well understood and is thus labeled with a question mark. The molecular nature of the replication-stalling lesion is not known.

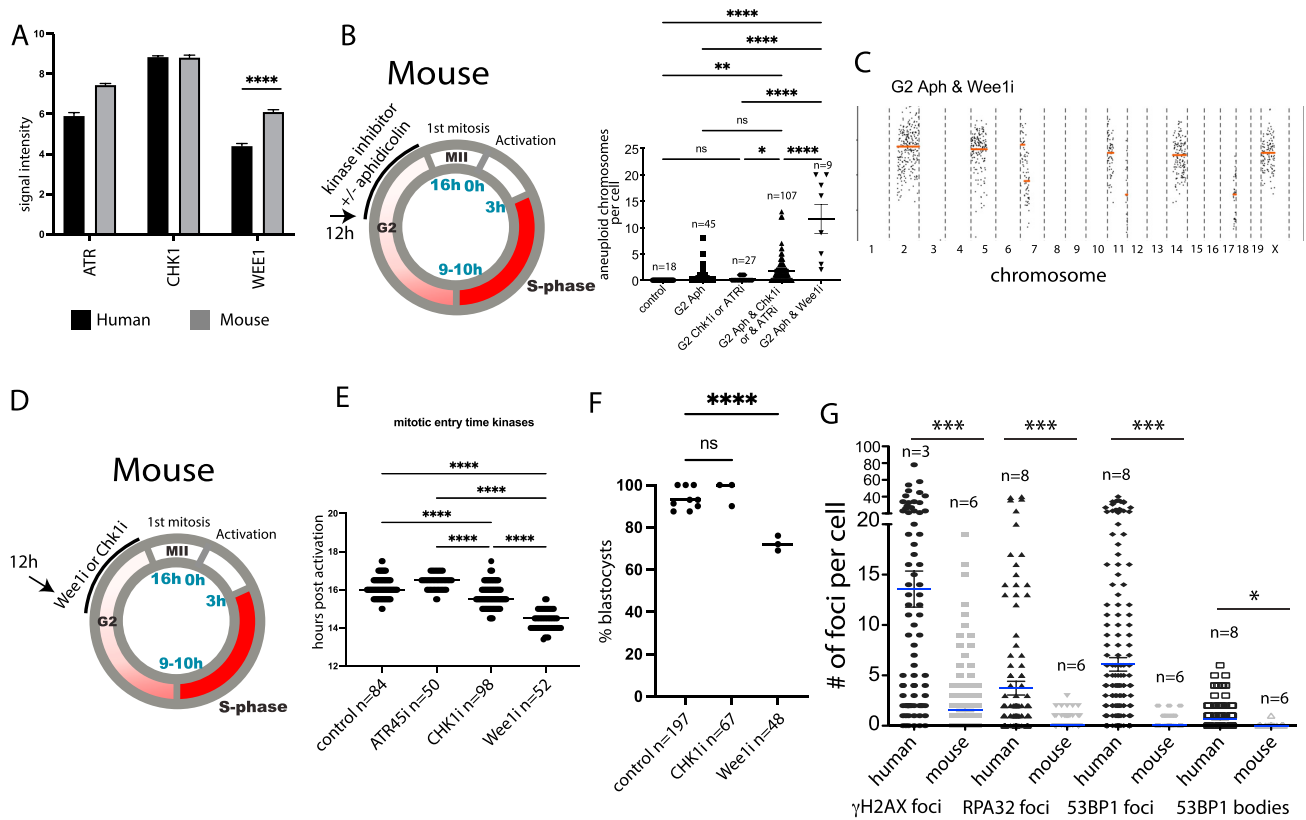


Figure S7. Mice show higher transcript levels of Chk1 and Wee1 kinases; mitosis is less sensitive to Chk1 inhibition than in humans but is highly sensitive to Wee1 inhibition, related to Figure 7

(A) Expression of checkpoint kinase transcripts in human and mouse 1-cell stage embryos. Data from Xie et al. (2010). Statistical analysis using Welch's t test, *** $p < 0.001$.

(B–F) Requirement for Wee1 kinase in the first G2 phase at the mouse 1-cell stage. (B) The experimental schematic and quantification of aneuploidies depending on the indicated condition. (C) The chromosome content plot after Wee1 inhibition combined with aphidicolin treatment showing aneuploidy and frequent chromosome breakage and segmental errors. (D) The schematic of treatment. (E) The timing of mitotic entry after indicated condition. (F) Developmental competence after treatment in first G2 phase with indicated inhibitors.

(G) Comparison of the frequency of markers of DSBs and repair in human and mouse embryos at the blastocyst stage. Note the significantly lower level of all markers in mouse embryos. Scale bars, 5 μ m. Statistical analysis using one-way ANOVA. *** $p < 0.0001$, ** $p < 0.001$, * $p < 0.01$.